A Quadratic Morphological Deep Neural Network Fusing Radar and Optical Data for the Mapping of Burned Areas

Seyd Teymoor Seydi, *Member, IEEE*, Mahdi Hasanlou, *Member, IEEE*, and Jocelyn Chanussot, *Fellow, IEEE*

***Abstract*—Wildfires are considered as one of the most disturbing factors in forest areas and high-density vegetation regions. The mapping of wildfires is particularly important for fire prediction and burned biomass estimation. Therefore, accurate and timely mapping of burned areas is of great importance and has a key role in disaster management. Estimation of burned areas from multispectral datasets is challenging, because of the complexity of the background and the different reflections of wildfires on the targets. To this end, this study presents a novel burned-area mapping framework based on the fusion of multitemporal Sentinel-1 coherence imagery and post-event Sentinel-2 imagery. The proposed framework uses hybrid quadratic morphological (QM) operations and convolution layers for deep feature extraction. The proposed architecture is known as the QMDNN-Net, where the overall framework of QMDNN-Net is based on a deep Siamese network. QMDNN-Net has double streams for extracting deep features from multitemporal coherence data and Sentinel-2 imagery. The streams are similar to each other and have the same number of group-dilated convolution blocks and QM layers. QMDNN-Net is defined based on quadratic dilation and erosion, and then it takes the average of these as output. The results of wildfire mapping with QMDNN-Net are evaluated here with two real-world wildfire datasets based on Sentinel-1 and Sentinel-2 imagery. The results show that QMDNN-Net achieves an overall accuracy and Kappa coefficient of 95.5% and 0.9, respectively, and outperforms other state-of-the-art methods.**

***Index Terms*—Burned area, convolutional neural networks, deep learning, morphological operator, sentinel-1, sentinel-2.**

I. Introduction

DUE to a number of factors such as climate change and human activities, wildfires have been occurring with greater frequency throughout the world [1]–[3]. Wildfires can damage the environment in different ways, such as through soil erosion and emission of greenhouse gases [4], [5]. Therefore, accurate and timely wildfire burned-area mapping is essential for further consequential analysis, such as wildfire prediction and estimation of burned biomass. Mapping of burned areas can be achieved according to two categories: traditional methods and remote-sensing satellite imagery. The use of earth-observation satellites is generally more popular because it has a number of advantages.

In recent decades, remote sensing has had a key role in the monitoring of the Earth for many applications [6]. Remote-sensing imagery can help with accurate and timely mapping at minimum cost and with large coverage. The diversity of remote-sensing imagery has resulted in its use in a wide range of applications, such as classification [7]–[9], change detection [10], [11], wildfire mapping [12], [13], and climate change [14], [15]. Among these, wildfire burned mapping (WFBM) is one of the important applications of remote-sensing imagery [16]. Many studies have included WFBM, such as for greenhouse-gas estimation from wildfires, burned-biomass estimation, wildfire damage assessment, and active wildfire detection [17].

With the increasing availability of remote-sensing imagery, WFBM has become a hot research topic, with many studies carried out to date (e.g., [18]). Burned-area mapping based on remote-sensing imagery can be applied to three main scenarios here:

1) bitemporal post/pre-event datasets;
2) post-event datasets;
3) fusion of heterogeneous datasets [19]–[21].

WFBM based on bitemporal datasets uses the change detection framework, with the similarities of pixels in the first and second datasets measured, and the generation of the WFBM based on a similarity value[16]. WFBM based on only post-events focuses on the difference in the spectral signatures of the pixels in the scene to detect "burned" pixels. The fusion scenario combines different types of remote-sensing imagery to detect burned pixels, which can then be applied based on combining previous scenarios [22].

A. Bitemporal Change-Detection-Based WFBM

Bitemporal change-detection-based WFBM is applied based on the detection of changes across prewildfire and postwildfire datasets. For instance, Hardtke *et al.* [23] designed a semi-automatic burned-area mapping framework in semi-arid ecosystem regions using time-series moderate resolution imaging spectroradiometer (MODIS) imagery. This framework was applied in three main steps:

Manuscript received March 8, 2022; revised April 28, 2022; accepted May 11, 2022. Date of publication May 16, 2022; date of current version June 2, 2022. *(Corresponding author: Seyd Teymoor Seydi.)*

Seyd Teymoor Seydi and Mahdi Hasanlou are with the School of Surveying and Geospatial Engineering, College of Engineering, University of Tehran, Tehran 1439957131, Iran (e-mail: seydi.teymoor@ut.ac.ir; hasanlou@ut.ac.ir).

Jocelyn Chanussot is with the Universite Grenoble Alpes, CNRS, GIPSA-Lab, Grenoble INP, 38000 Grenoble, France, and also with the Aerospace Information Research Institute, Chinese Academy of Sciences, Beijing 100094, China (e-mail: jocelyn.chanussot@grenoble-inp.fr).

Digital Object Identifier 10.1109/JSTARS.2022.3175452

1) generation of the time-series normalized burned ratio (NBR);
2) detection of potentially burned pixels using change detection by image differencing between time (n)th and (n-1)th;
3) segmentation in a region-growing manner, then visualisation and vectorisation of the detected wildfire areas.

Hawbaker *et al.* [24] proposed burned-area detection to produce the "Landsat burned-area essential climate variable product" using dense time-series data. They applied the algorithm using a gradient-boosted regression model to estimate the probability of burned areas in scenes from Landsat data. Next, the maximum burned probability value was generated by compositing the burned probabilities with the time-series dataset. The final binary burned map was generated using the segmentation process and thresholding. Jakimow *et al.* [25] presented a fire-detection and tillage-events framework based on dense time-series Landsat-7 and Landsat-8 datasets. This procedure was applied in four main steps:

1) extraction of three clear Landsat observation sequences (at the acquisition date, and before and after the acquisition date);
2) model parameterisation and classification based on a random forest algorithm;
3) aggregation of random forest class probabilities for each year, to estimate the class score;
4) derived annual layers summarised as single annual maps that show the burned and tilled areas.

Giglio *et al.* [26] proposed a burned-area mapping framework based on a daily time series MODIS dataset. This method was applied in a series of steps:

1) extraction of daily surface reflectance and active fire masks;
2) generation of change/fire-related composites;
3) extraction of temporal texture, which uses the local standard deviation;
4) selection of training sample based on a cumulative active-fire composite;
5) extraction of conditional probability densities for burned and unburned sample data using a Gaussian kernel estimator;
6) separability test applied for burned and unburned conditional probability distributions, to ensure they differ considerably;
7) prior probabilities that establish spatially explicit prior burned probabilities;
8) posterior burned probability used to give the observed change in a vegetation index;
9) initial classification to generate the experimental classification of burned or unburned;
10) final classification based on additional contextual information and a majority filter.

Roteta *et al.* [27] developed a two-stage burned-area mapping system based on bitemporal Sentinel-2 imagery and the MODIS MCD14ML fire product. Initially, the burned areas were detected based on a fixed threshold for the spectral burned indices, and then this was overlaid with the MCD14ML hotspots at the same time. The burned areas obtained by the first step were used to estimate tile-dependent statistical thresholds for each predictive variable, which were applied in a two-step manner. Lizundia-Loiola *et al.* [28] developed a global burned-area mapping procedure by combing near-infrared reflectance bands and active fire information that originated from MODIS. This method was applied in two phases: detection of high potential burned pixels based on the thresholding of spectral indices by mixing the thermal and reflectance bands, and growth of the contextual region for reducing the omission errors and detection of the burned patches. Pinto *et al.* [29] proposed a deep-learning-based burned-area detection method based on the visible infrared imaging radiometer suite (VIIRS) dataset. The proposed framework was based on U-Net architecture that used the three-dimensional convolution layers and long short-term memory in the encoder parts. Furthermore, the transpose convolution and temporal convolution layers were used in the decoder part. Liu *et al.* [30] presented a burned-area detection model based on time series Landsat data and harmonic model fitting. This method was initially applied to the "Breaks for the Additive Season and Trend" monitor for segmentation of stable periods. Then, the harmonic model was fitted for a stable period using the time series burned-area index. Burned-area detection was achieved by comparing the predicted value by the model and the observed value based on a threshold. Seydi *et al.* [16] presented a burned-area mapping framework based on bitemporal Sentinel-2 imagery using Google Earth Engine cloud computing. This framework was applied in three stages:

1) extraction of spectral and spatial features for the bitemporal dataset;
2) change detection based on image differencing;
3) burned-area detection based on binary classification using a random forest algorithm.

Llorens *et al.* [31] proposed a burned-area detection method using Sentinel-2 imagery based on the detection of changes by NBR indexing and thresholding. The threshold values were defined by the European Forest Fire Information Service algorithm. Furthermore, this method can generate the burned severity level according to the separability index.

B. Post-Event-Based WFBM

WFBM can be applied based on an investigation of the reflection of the burned area. Thus, burned areas have different characteristics compared to unburned areas. Therefore, WFBM methods are designed to detect burned areas based on comparisons of spectral features of burned areas with the background. For example, Urbanski *et al.* [32] presented a burned-area detection method that combined a VIIRS active fire and burn scar identification model. This framework was applied in two steps: 1) use of a burned-scar detection model based on the spectral ratio of the top of atmosphere reflectance VIIRS infrared M-bands, to detect the high potential burned-scar pixels; and 2) use of a contextual filter to refine the classified pixels based on VIIRS I-band active fire detection. Furthermore, Cabral *et al.* [33] considered the potential of genetic programming methodologies for burned-area mapping using the Landsat ETM+ imagery. They compared the results of burned mapping with two classical

methods: maximum likelihood classification and classification and regression tree analysis. The results of the mapping showed that genetic programming had a high efficiency compared to the other two methods. Additionally, Çömert *et al.* [34] designed an object-oriented burned-area mapping procedure based on multiresolution segmentation and a random forest algorithm. They applied the proposed framework to Landsat-8 satellite imagery. Furthermore, they used the spectral burned indices (i.e., burned-area index, normalized burned index) and vegetation indices (i.e., normalized difference vegetation index [NDVI], enhanced vegetation index) to enhance their burned-area mapping results. Moreover, Brand and Manandhar [35] used a semantic segmentation-based method for burned-area mapping with mono-temporal Sentinel-2 imagery. The U-Net-based segmentation deep learning framework has also been used for burned-area mapping. The performance of the proposed method was tested in different areas, and the accuracy assessment showed that the proposed method had high generalization despite highly diverse objects. In addition, Sertel and Alganci [36] evaluated the performance of a pixel-based and object-based burned-area detection method using the SPOT-6 dataset. They used the spectral bands and NDVI for the classification of burned areas. A rule-based classifier was used to classify the segments, and a maximum likelihood classifier was used for pixel-based classification. The results of this classification showed that object-based classification has high efficiency compared to pixel-level classification. Ngadze *et al.* [37] evaluated the contribution of spectral bands on the performance of burned-area mapping using a random forest classifier. They used post-fire Sentinel-2 and Landsat-8 satellite imagery to map burned areas. The outcome of this burned-area mapping was illustrated using four spectral bands (i.e., blue, red, red-edge, near-infrared) and had a high contribution to the of mapping burned areas. Moreover, Dragozi *et al.* [38] investigated the impact of spectral/spatial features on burned-area mapping using a very high-resolution IKONOS dataset. They conducted the experiments in two steps: pixel-level classification and object-level classification. They used the "fuzzy complementary criterion" to select the features and a support vector machine algorithm as a classifier. The results of this mapping showed that object-level classification has greater accuracy than pixel-level classification. Furthermore, the feature selection method can improve the results and reduce the computational costs. Ba *et al.* [39] developed a burned-area mapping framework based on spectral indices and a back-propagation neural network. This framework was applied in three phases

1) sample data generation as five classes (i.e., vegetation, cloud, bare soil, burned area, shadow) based on an empirical formula method, a multithreshold technique, and a visual interpretation algorithm;
2) Spectral characteristics analysis based on separability index M to assess the burned and unburned classes;
3) a back-propagation neural network for mapping burned areas using the sample data generated.

Knopp *et al.* [40] presented a semantic segmentation-based method based on U-Net architecture for mapping burned areas. They used the post-fire mono-temporal Sentinel-2 satellite imagery to map the burned areas. They also assessed the efficiency of the spectral bands to map burned areas, whereby visible, near-infrared, and shortwave infrared provided high contributions to the mapping of the burned area. Wang *et al.* [41] developed super-resolution burned-area mapping based on space–temperature information and Sentinel-2 satellite imagery. The space–temperature information had two elements: a space element that used a random walker algorithm to obtain the space element with highly detailed space information and a temperature element that provided rich temperature information that was obtained by calculating the NBR index. These elements were then integrated to generate an objective function with space–temperature information. Finally, a particle swarm optimization algorithm was used to optimize the objective function, and then the burned-area mapping result was generated.

C. Fusion-Based WFBM

Fusion-based WFBM focuses on multimodal datasets and takes advantage of the different datasets to provide high efficiency. For example, Zhang *et al.* [42] proposed a deep-learning-based framework for mapping burned areas using the synergy of the Sentinel-1 and Sentinel-2 imagery. The proposed deep-learning-based framework was based on Siamese self-attention architecture that uses a self-attention module and a convolution layer. For mapping burned areas, this method uses bitemporal Sentinel-2 imagery, time-series coherence and backscatter (γ_0), and bitemporal NDVI. Additionally, Boschetti *et al.* [22] fused MODIS and Landsat ETM+ to map burned areas on a large scale, with a spatial resolution of 30 m. This method was applied in three main steps

1) detection of high potentially burned pixels based on decision-tree-based semantic change detection, by examination of a spectral category time series using Landsat imagery;
2) generation of candidate burned objects based on segmentation of detected high potential pixels using temporal and spatial proximity criteria;
3) making a decision on candidate burned objects by examination of the contemporaneous 1 km MODIS active fire detection.

Moreover, Alonso-Canas and Chuvieco [43] developed a two-step global burned-area mapping method using time series of the "medium resolution imaging spectrometer" data and thermal information derived from the MODIS hotspot product. This method used cumulative distribution functions to separate burned pixels. In the next step, a contextual criterion was used to enhance the spatial detection of the burned patches from the seed pixels. Furthermore, Roy *et al.* [44] designed a burned-area mapping algorithm based on combining the Landsat-8 and Sentinel-2 datasets. The fusion process was applied by random forest change regression that was trained with synthetic data built from laboratory and field spectra and used a spectral model of fire effects on reflectance. The random forest algorithm was applied to each pixel on a temporal rolling basis considering 3 months of sensor data, to map the central month. A temporal consistency check was used to minimize commission errors derived from

nontarget changes. Furthermore, a region-growing technique was used to handle omission errors. In addition, Belenguer-Plomer *et al.* [45] designed a detection-based framework to map burned areas using Sentinel-1 and hotspots originating from MODIS and VIIRS sensors. This framework used the Reed-Xiaoli detector algorithm to detect anomalous changes in the backscatter coefficient dataset. These changes were overlaid with hotspots, which helped to enhance the burned-area mapping. Furthermore, a random forest classifier was used for some areas where ancillary data were not available. Also, a land-cover map was used to improve the performance of the Reed-Xiaoli algorithm. Crowley *et al.* [46] presented a wildfire progression system based on multisensor datasets (i.e., MODIS, Sentinel-2, Landsat-8). This method initially generated the provisional classifications by change detection based on the bitemporal NBR index. Then, Bayesian updating of a land cover algorithm was used to combine the results of the burned classification maps, which were derived from multisensors. Finally, Belenguer-Plomer *et al.* [47] designed a deep-learning-based framework for the mapping of burned areas using Sentinal-1 and Sentinel-2 imagery. They used the multitemporal γ_0 of the Sentinel-1 dataset and the multitemporal spectral indices of the Sentinel-2 dataset as inputs for convolutional neural networks (CNNs).

Although many studies have designed several algorithms for mapping burned areas and have developed them for specific types of satellite imagery (e.g., MODIS, Landsat, VIIRS, Sentinel), many limitations remain, as follows.

1) Most methods have used the active fire products, while there is strong uncertainty in mapping active fires. Moreover, the accuracy of the methods mentioned depends absolutely on the quality of the hotspot maps, and the hotspot products generally have low spatial resolution that might not be detected by the algorithm.
2) Spatial resolution is the most important challenge among these methods. However, coarse spatial resolution for mapping burned areas over wide coverage is not of great importance, but for small areas, it is the most important factor. Therefore, mapping burned areas for small areas using coarse resolution datasets is a big challenge and can even be impossible.
3) Change-detection-based methods require more consideration because the changes can be derived from other factors, such as vegetation growth, tree felling, and agricultural harvesting. Moreover, due to some environmental conditions (e.g., cloudy) and poor temporal resolution, finding a pre-event dataset can be very difficult.
4) Most methods are based on manual features generation based on spectral features (e.g., NBR, NDVI), while they ignore the potential of spatial features in the mapping of burned areas. Additionally, manual feature generation and selection of suitable features are time-consuming, especially for large-scale areas.
5) Most methods have used conventional classifiers, such as random forest or maximum likelihood classifiers, while advanced classifiers can guarantee that reliable results will be obtained. These above-mentioned methods are based on thresholding spectral indices or original spectral bands. A single threshold value is, however, not effective, due to the complexity of the background and the ecosystem characteristics.

To minimise these challenges, the present study presents a novel framework for mapping burned areas. This framework can cover the limitations of current burned-area mapping methods. This proposed method is termed the QMDNN-Net method, and it is applied based on the fusion of Sentinel-1 and Sentinel-2 datasets, which have many advantages compared to other state-of-the-art methods. The QMDNN-Net method combines multiscale convolution blocks and learnable morphological layers, and it can extract the linear and nonleaner deep features to improve the results of burned-area mapping in more complex areas. These advantages mean that the QMDNN-Net method can map burned areas with high accuracy and low error rates. Also, the efficiency of the fusion of the synthetic aperture radar (SAR) and optical datasets into a single dataset gains the maximum advantage of the fusion datasets.

Deep-learning-based methods that can automatically extract deep features by convolution layers have provided promising results, which has converted this into a hot topic research area. Convolution layers have a key role in the generation of the deep features, such that many kinds of convolution layers have been developed (e.g., standard convolution, dilated convolution). However, standard convolution layers do not have a high capacity for capturing scaled or rotated objects, while this can be provided by data augmentation. One advanced deep-feature extractor method is learnable morphological scale-space layers. Unlike standard convolution layers, the morphological scale-space operators can also extract nonlinear features, and they are equivariant to some transformations (e.g., rotation, affine transformation, scaling). The efficiency of morphological scale-space operators to increase the generalisation of deep-learning methods has been shown. Recurrently, the morphological neural network is taken into consideration, as this can provide promising results for some applications. Here, we combined the quadratic morphological (QM) operations with a standard convolution layer to enhance the performance of the network for solving nonlinear burned-area mapping in highly complex areas.

The main contributions of this research are following.

1) We deeply revisit WFBM methods and their problems and propose a novel deep-learning framework that combines the morphological learnable scale-space operations (i.e., quadratic dilation, quadratic erosion) and the group-dilated-convolution (GDC) block for the first time.
2) We introduce a QM empirical mode (QMEM) based on two morphological operators for greater exploration of deep features.
3) We take advantage of the temporal coherence map and post-event optical datasets for accurate mapping of burned areas.

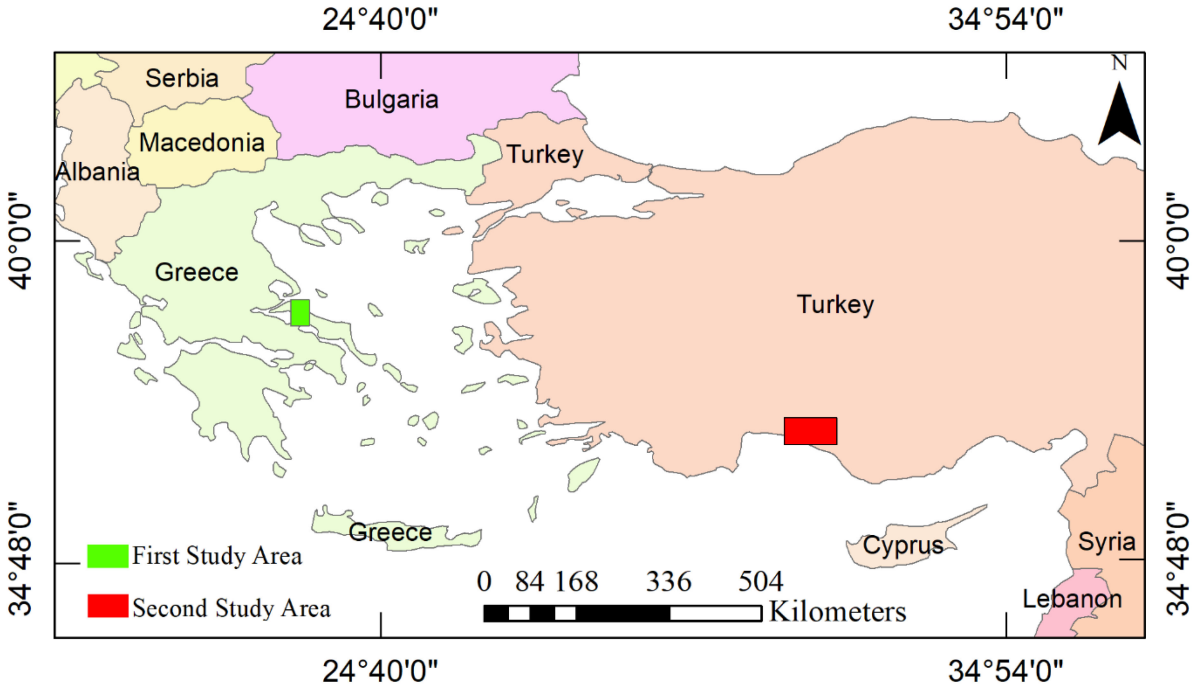

Fig. 1. Locations of the two study areas for the burned-area mapping.

4) We evaluate the potential of the multispectral and multitemporal coherence SAR datasets for mapping burned areas and compare the results with state-of-the-art methods.

The rest of this article is organized as follows. Section II introduces the study areas and the datasets. Section III gives the details of the QMDNN-Net for burned-area mapping. The evaluation results are provided in Section IV and are discussed in Section V.

II. Case Study and Satellite Images

A. Study Area

This study used two large covered wild wildfire areas located in different areas. The first study area was located on Evia Island (Greece), which is the second-largest island (see Fig. 1). This fire started on 3 August, 2021, and was intensified by strong winds. The second study area was located in the southern part of Turkey, in the Antalya province (see Fig. 1). This disaster began in July 2021, and lasted for many days.

B. Satellite Images

This study used the post-fire Sentinel-2 dataset for mapping the burned areas. The Sentinel-2 mission consists of two satellites (Sentinel-2-A, Sentinel-2-B) that collect data with a temporal resolution of 5 days. The Sentinel-2 sensors have 13 spectral bands with different spatial resolutions (10, 20, 60 m). This study used the spectral bands with spatial resolution of 10 and 20 m. Furthermore, the Level-2A product was used for the next analysis that was preprocessed (i.e., atmospheric correction).

The Sentinel-1 satellites are equipped with C-band SAR that captures the data with four operational imaging modes of different spatial resolutions. Sentinel-1 has two sensors (Sentinel-1A, Sentinel-1B) that were launched in April 2014 and April 2016 (respectively). This study used the multitemporal single look complex with interferometric wide swathe mode for the WFBM.

C. Datasets

This study fused the multitemporal Sentinel-1 SAR dataset and the post-fire Sentinel-2 optical dataset for mapping the burned areas. The Sentinel-1 datasets needed to be preprocessed to generate the multitemporal coherence map. We used the SANP open-source software for preprocessing the Sentinel-1 data, to produce the coherence map. After preprocessing, and according to the flowchart presented in Fig. 4, the multitemporal coherence maps generated two polarisations (VV, VH). Figs. 2 and 3 show the incorporated Sentinel-2 dataset and multitemporal coherence maps generated for the first and second datasets, respectively.

This study was conducted experimentally in two different areas with wide coverage. The details of the incorporated datasets for the two study areas are presented in Table I. The Sentinel-2 dataset includes some spectral bands that had a spatial resolution of 20 m.

III. Methodology

The proposed framework for the QMDNN-Net method is applied in three steps according to the flowchart in Fig. 4. The first step is the preparation of the data (which have some preprocessing applied) and coherence map generation. The second step is the training phase, where the model parameters are tuned by

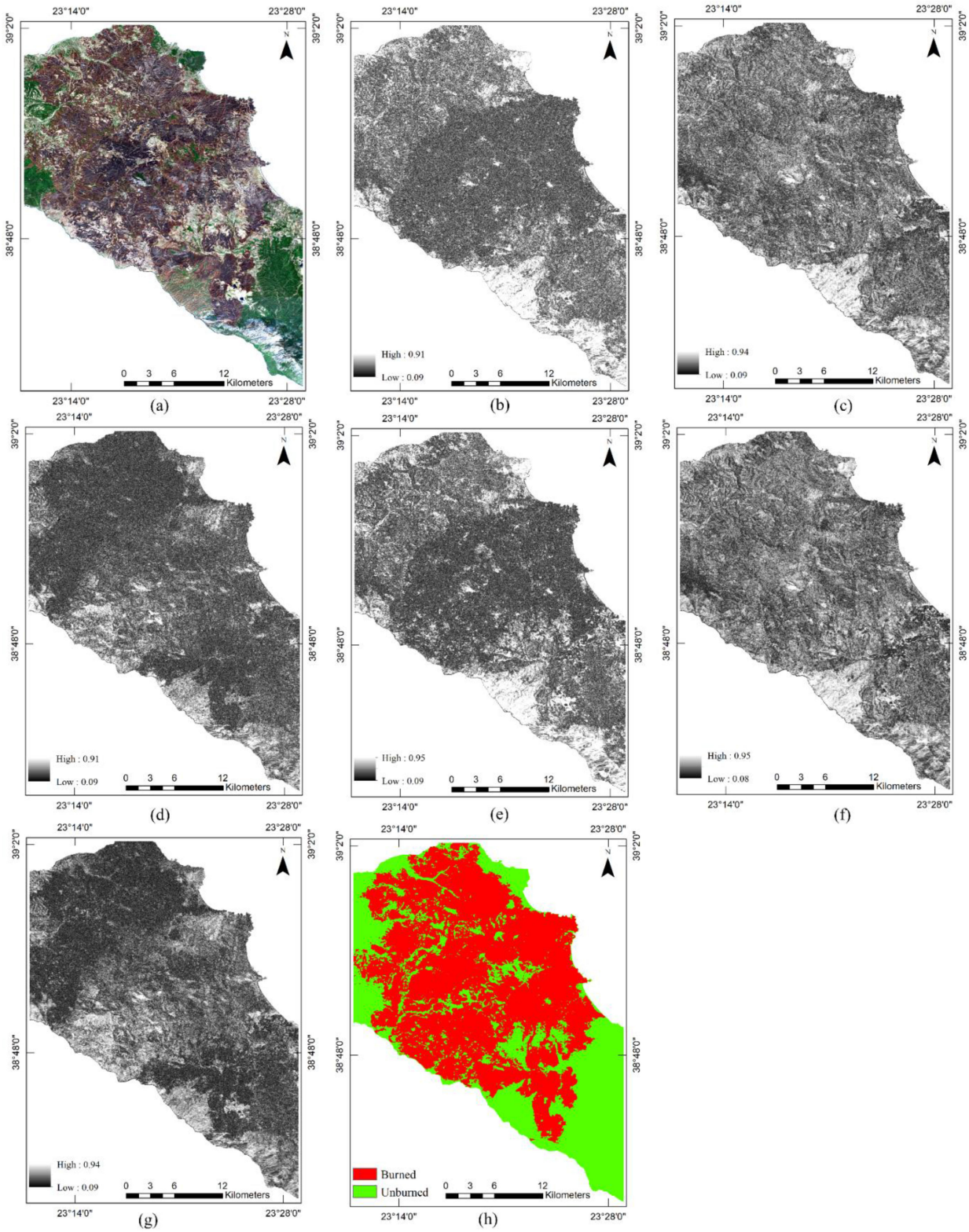

Fig. 2. Dataset used in the WFBM for the first study area. These included (a) the post-event Sentinel-2 imagery, (b) the coherence maps generated, as VH time-1, (c) VH time-2, (d) VH time-3, (e) VV time-1, (f) VV time-2, (g) VV time-3, and (h) the ground truth.

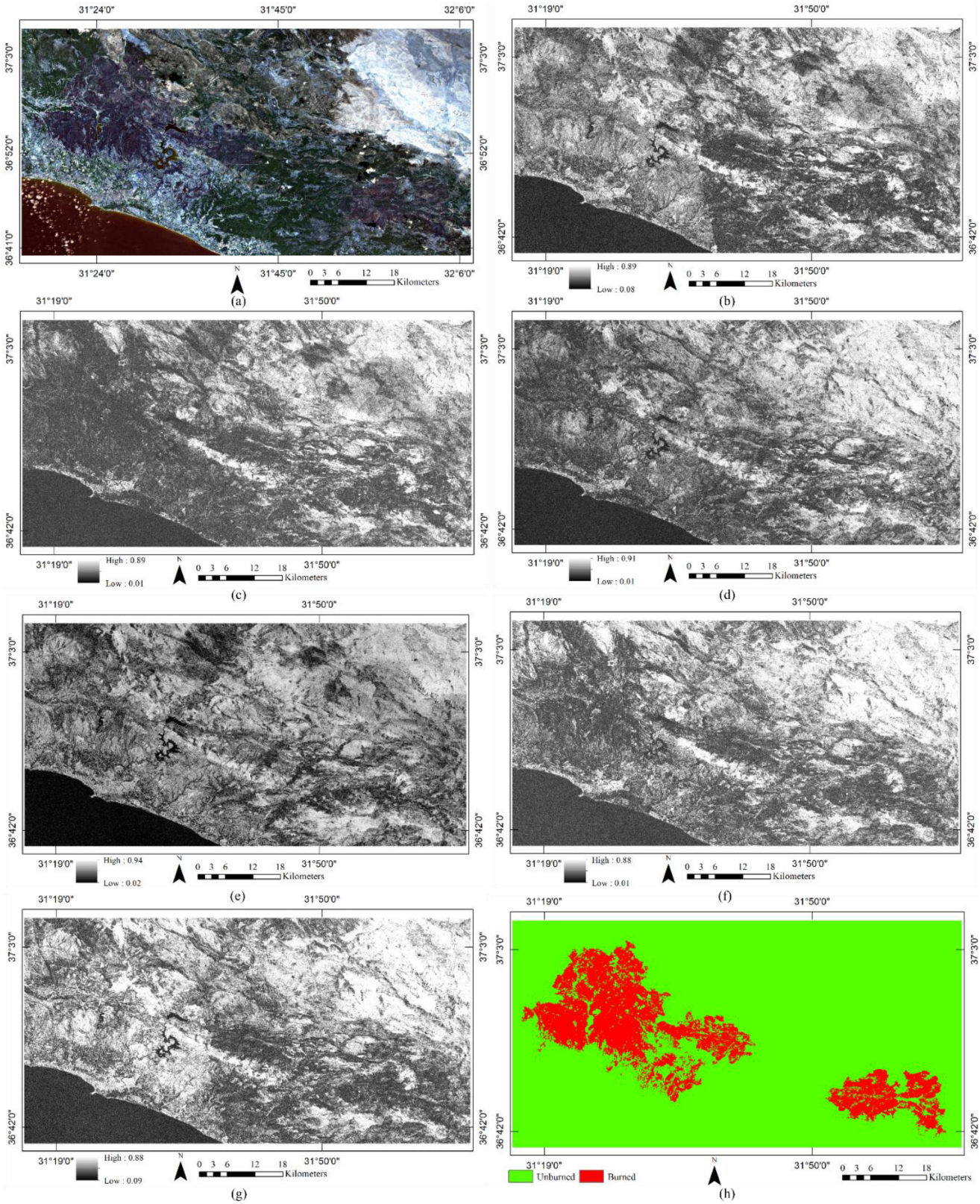

Fig. 3. Dataset used in WFBM for the second study area. These included (a) the post-event Sentinel-2 imagery, (b) the coherence maps generated, as VH time-1, (c) VH time-2, (d) VH time-3, (e) VV time-1, (f) VV time-2, (g) VV time-3, and (h) the ground truth.

TABLE I
MAIN CHARACTERISTICS OF THE INCORPORATED DATASETS FOR THE TWO STUDY AREAS

Sensor	Property	Study areas	
		First	Second
Sentinel-2	Spectral bands	10	10
	Spatial resolution (m)	10	10
	Data size (pixel)	3353×4759	9647×4872
	Pre-event acquisition date	August 2021	August 2021
Sentinel-1	Polarisation	VV, VH	VV, VH
	Spatial resolution (m)	10	10
	Data size (pixel)	3353×4759	9647×4872
	Pre-event acquisition date	July 2021	July 2021
	Post-event acquisition date	August 2021	August 2021

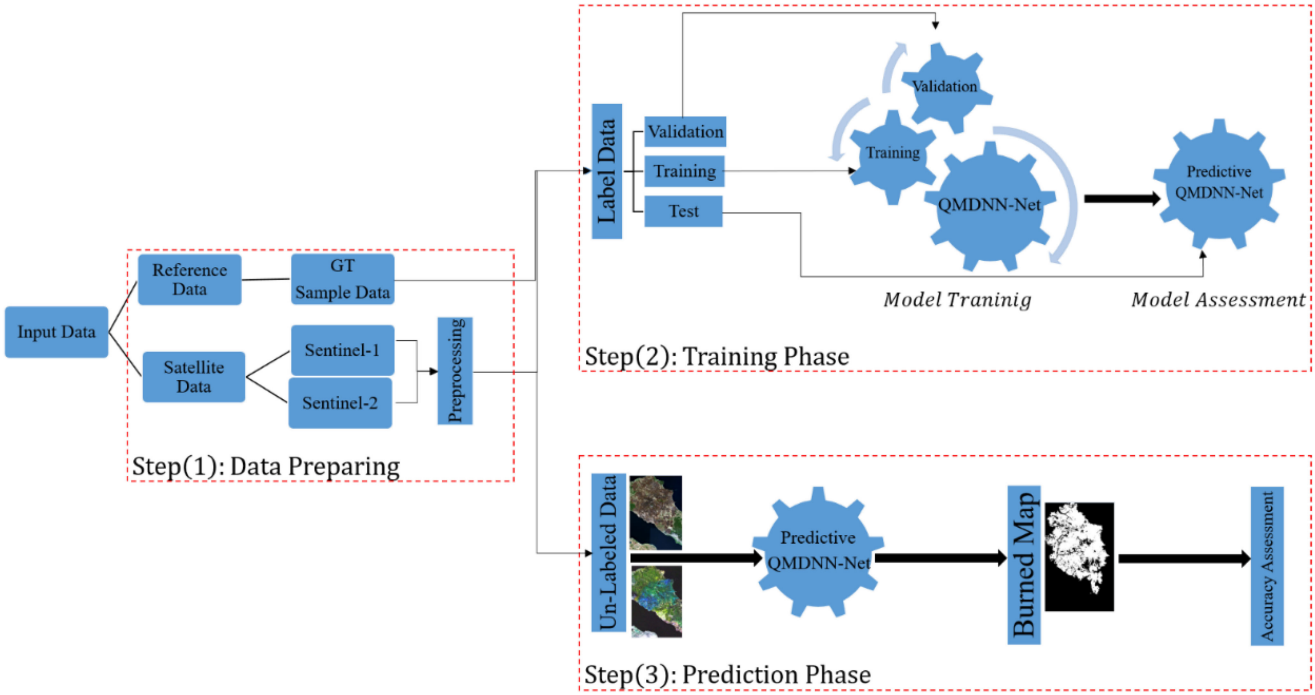

Fig. 4. Overview of the general framework for WFBM.

training and validation data, and then assessed by testing data. The last phase is the prediction phase, where unlabelled data are fed to the model to predict the burned areas.

A. *Preprocessing*

The preprocessing is the first step in the QMDNN-Net method, which is applied separately to the Sentinel-1 and Sentinel-2 datasets. The most important preprocessing of the Sentinel-2 dataset is an atmospheric correction to convert top-of-atmosphere to surface reflectance. The atmospheric correction was carried out using the *Sen2Cor* processer that is available in the open-source SNAP software [48], [49].

The Sentinel-1 interferometric wide swath mode acquisitions in the single look complex product format were used for the WFBM. This product has several main steps of preprocessing: TOPSAR-spilt; apply orbit file; back-geocoding; enhance spectra diversity; coherence generation; TOPSAR-deburst; and multilook and terrain correction [50], [51]. The Sentinel-1 data processing is carried out via the SNAP software platform. The complex coherence quantifies the relative stability of the scattering mechanisms within a window between two SAR acquisitions [52]. The complex coherence (γ) is between 0.0 and 1.0, and for two coregistered complex signals of SAR images it is estimated using (1) [50], [53]

$$\gamma = \frac{E\langle s_1 . s_2{}^{*}\rangle}{\sqrt{E\langle |s_1|^2\rangle . E\langle |s_2|^2\rangle}} \tag{1}$$

where s_1 and s_2 are complex signals of the SAR datasets, $E\langle . \rangle$ is the expectation operator, $*$ indicates the complex conjugate, and $|.|$ indicates the absolute operator. In practical applications, we use the coherence ensemble average ($\hat{\gamma}$) instead of the measurement of the mathematical expectation of SAR signals,

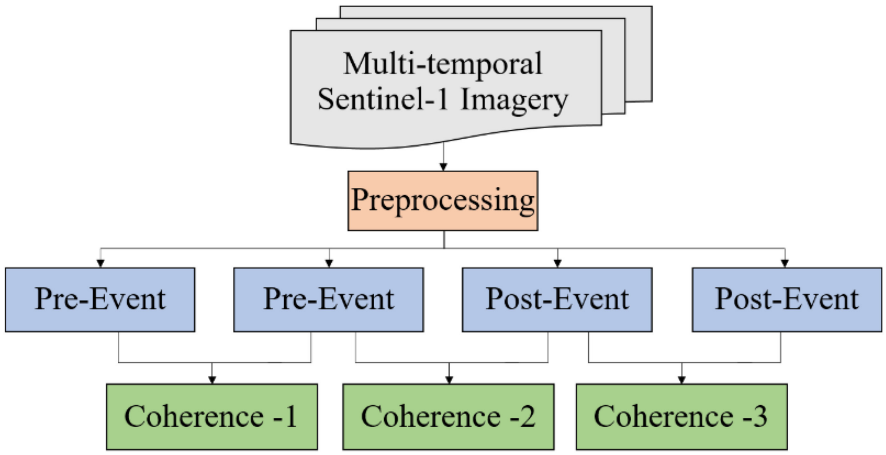

Fig. 5. Multitemporal coherence map generation procedure.

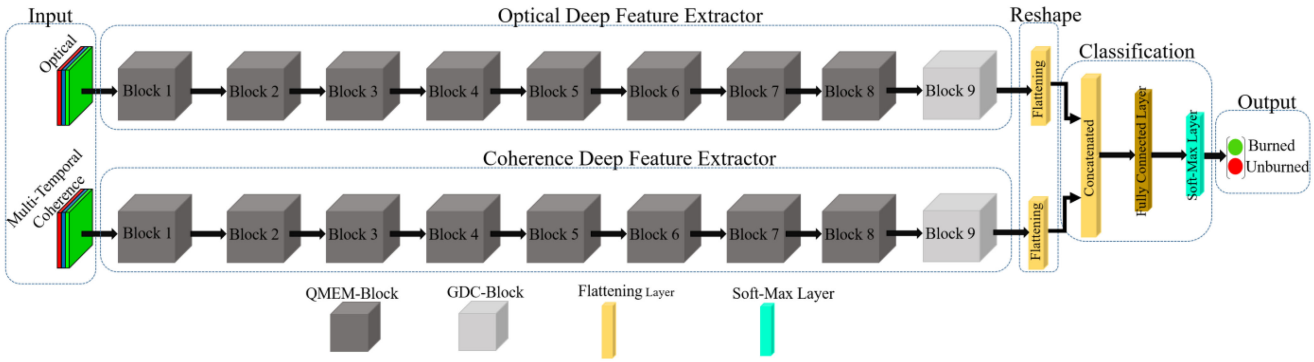

Fig. 6. Overview of the QMDNN-Net method architecture for WFBM (burned-area mapping).

which can be defined as

$$\hat{\gamma} = \frac{\left|\sum_{i=1}^{N} s_{1i} \cdot s_{2i}^{*} \cdot e^{j\varphi(i)}\right|}{\sqrt{\sum_{i=1}^{N} |s_{1i}|^2 \cdot \sum_{i=1}^{N} |s_{2i}|^2}} \tag{2}$$

where N is the number of pixels in the window. The coherence map of each new image is generated with respect to the previous image. An overview of the multitemporal coherence map generation is shown in Fig. 5.

B. Proposed Deep-Learning Architecture

The architecture of the QMDNN-Net method for WFBM is shown in Fig. 6. Based on this architecture, QMDNN-Net was built from six parts, which included

1) the input part;
2) the deep feature extraction stream based on the optical dataset;
3) the deep feature extractor channel from the multitemporal coherence dataset;
4) the reshaping of deep features by flattening layers;
5) the classification part;
6) the output.

The input of QMDNN-Net is patch data with a defined size, which is set at 13×13 for each deep feature extractor stream. Next, the input patch data is fed to deep feature extractor streams to explore the higher level and more effective deep features. The deep feature extractor streams are the same in terms of structure and number of layers. The deep features are extracted by hybrid QM layers and GDC blocks. Then, the deep feature reshapes by flattening the layer to be transferred to the classification part. The deep features are integrated by concatenating the layers and feeds to fully connected layers. Finally, the soft-max layer is used to decide on the input patch data. The main differences between the proposed QMDNN-Net method architecture with other CNN frameworks are following.

1) Use of the trainable morphological scale-space layers, which can increase the efficiency of the network for the extraction of nonlinear features. Furthermore, they dramatically improve the generalisation to unseen scales compared to standard convolution layers.
2) Combination of the GDC-block for more exploration and increased robustness of the network with the morphological scale-space operator. Another advantage of the GDC-block is the exponential expansion of the receptive field without loss of resolution.

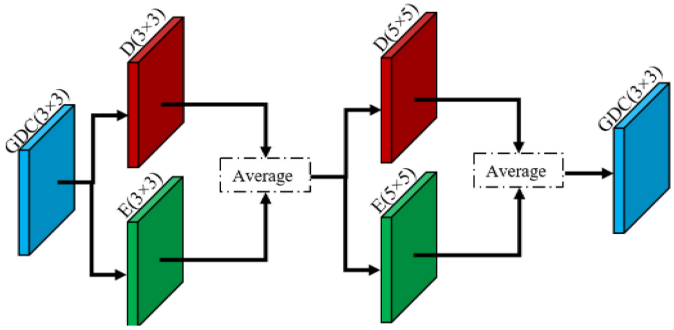

Fig. 7. Structure of the QMEM-block.

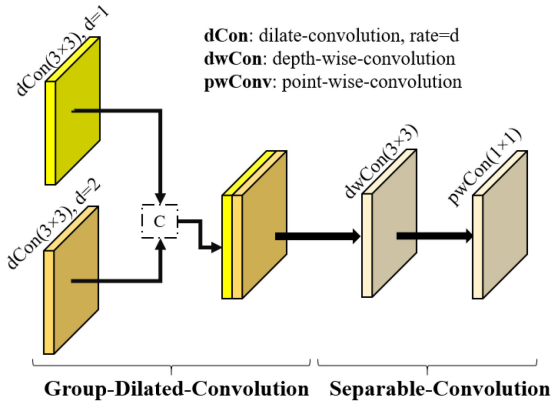

Fig. 8. Structure of the GDC-block.

3) Taking advantage of the QMEM-block based on two morphological operators for more exploration of deep features.
4) Use of separable convolution layers, which reduces the number of parameters of the network without reducing the effectiveness.

C. QMEM-Block

The empirical mode decomposition is a fully data-driven algorithm designed for linear and nonstationary time series analysis that has been introduced recently by Huang *et al.* [54]. This method is considered as a simple and robust multiscale decomposition technique that is widely used in many applications. The main idea behind empirical mode decomposition is to decompose original real data into a number of oscillatory modes called intrinsic mode functions. The empirical mode decomposition uses lower and upper envelopes of the signal in an iterative decomposition manner, for representing a signal. The empirical mode decomposition can be formulated based on pairs of morphological operators. Thus, this research uses the quadric morphological operators (erosion and dilation operator) for formulation of empirical mode decomposition. The QMEM can be defied based on QM erosion (ε_{q_τ}) and (δ_{q_τ}) and dilation operators as defined based on the following [55]:

$$\text{QMEM} = \frac{\varepsilon_{q_\tau}(f)(x) + \delta_{q_\tau}(f)(x)}{2}. \tag{3}$$

The QMEM-block has a key role in the QMDNN-Net method for the extraction of deep features for WFBM. This structure is based on quadratic dilation and erosion operators and then averaging. The structure of the QMEM-block is shown in Fig. 7, which includes quadratic dilation and erosion operators and two dilated group convolution blocks. Four steps are involved in applying the QMEM-block.

1) Employing the GDC block on the previous layer of the features map.
2) Using two QM operators with kernel size (3×3).
3) Applying two QM operators with kernel size (5×5) to the extracted features from step (2).
4) Using GDC-Block to explore the data further.

This QMEM-block uses two QM operators with different kernel sizes (i.e., 3×3, 5×5).

The structure of the GDC-block is shown in Fig. 8, which contains two convolution layers with different dilation rates (i.e., 1, 2). Then the extracted features are concatenated and fed to a separable convolution layer. The separable convolution layer has built two point-wise and depth-wise convolution layers.

D. Convolution Layer

Mathematically, the feature value (Ψ) in the *l*th layer is expressed using (4) [56]

$$v^l = g\left(w^l x^{l-1}\right) + b^l \tag{4}$$

where x is the input data, g is the activation function; b is the bias vector for the current layer, and w is the weighted vector. The value (v) at position (x,y) on the *j*th feature *i*th layer for the two-dimensional convolution layer is given as [57]

$$v_{i,j}^{xy} = g\left(b_{i,j} + \sum_{\chi}\sum_{\omega=0}^{\Omega_i-1}\sum_{\varphi=0}^{\Phi_i-1} W_{i,j,\chi}^{\omega,\varphi} v_{i-1,\chi}^{(x+\omega\times d_1)(y+\varphi\times d_2)}\right) \tag{5}$$

where χ is the feature cube connected to the current feature cube in the $(i-1)$th layer, Ω and Φ are the length and width of the convolution kernel size, respectively, and d_1 and d_2 are the dilation rates, as length and width, respectively. Fig. 9 shows the main difference between standard convolution and depth and point-wise convolution. The separable convolution was built using point-wise [see Fig. 9(b)] and depth-wise [see Fig. 9(c)] convolution.

E. QM Layer

Morphological operators are considered as nonlinear operators that are focused on the spatial structure of the images [58], [59]. *Erosion* and *Dilation* are the basic mathematical morphological shape-sensitive operations [60], [61]. These operators can extract discriminative spatial–contextual information during the training stage [62]. Let f be the image data that can be represented as a function where the intensity at position x is represented by $f(x)$; thus, the *Erosion*(ε_b) and *Dilation*(δ_b) can be defined for f as [60]–[63]

$$\varepsilon_b(f)(x) = \min_{i\in[-n,n]}(f(x+i) - b_i) \tag{6}$$

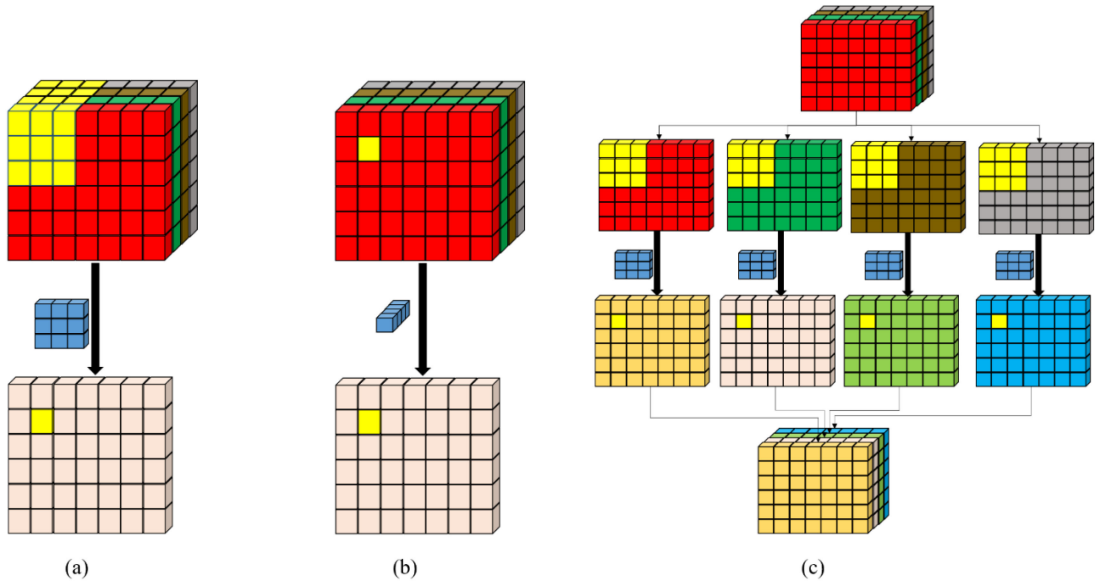

Fig. 9. Main differences between standard convolution and separable convolution (point-wise and depth-wise). (a) Standard convolution. (b) Point-wise convolution. (c) Depth-wise convolution.

$$\delta_b(f)(x) = \overset{min}{i\in[-n,n]}(f(x-i)+b_i) \tag{7}$$

where b is the structure element. Based on the theory of morphological scale spaces, the saleable nonflat structure functions are the most valuable functions [64]–[67]. Assume $\tau_{\mathrm{n\times n}}$ is a symmetric positive definite matrix, and thus the quadratic structuring function associated with the τ matrix is denoted as q_χ and is as defined as (8) [55]

$$q_\tau(\alpha) = -\frac{1}{2}\langle\alpha, \tau^{-1}\alpha\rangle. \tag{8}$$

This equation for a separable and rotationally invariant structuring function can be simplified as

$$q_\tau(\alpha) = -\frac{\|\alpha\|^2}{2\tau}. \tag{9}$$

The erosion and dilation by the quadratic structuring function are denoted by ε_{q_τ} and δ_{q_τ}, respectively, which are defined as

$$\varepsilon_{q_\tau}(f)(x) = \inf_{z\epsilon E}\left\{f(\alpha-x)+\frac{\|\alpha\|^2}{2\tau}\right\} \tag{10}$$

$$\delta_{q_\tau}(f)(x) = \inf_{z\epsilon E}\left\{f(\alpha+x)-\frac{\|\alpha\|^2}{2\tau}\right\}. \tag{11}$$

F. Classification

The classification task can be applied by a multilayer perceptron classifier, which is applied to the extracted deep features. The multilayer perceptron classifier is composed of a fully connected and soft-max layer. The output deep features extractor part reshapes the layer by flattening it, and then feeds it to a fully connected layer. The fully connected layer connects the deep feature extractor parts to the soft-max layer. The soft-max layer is the last layer in the multilayer perceptron classifier, as an activation function is used to assign the probabilities belonging to each class for the input patch.

G. Training Process

While the parameters of the network are, thus, optimized iteratively by an optimizer, the adaptive moment estimation optimizer was used to tune the network parameters [68]. The QMDNN-Net is initialized by He-Normal by an initializer, and then the model is trained. Next, the error network is calculated by a loss function in the training process, and the error value is fed to the optimizer to update the network parameters by back-propagation. The Tversky loss function was used to estimate the loss of QMDNN-Net in the training process [69]. The Tversky index between $\hat{v}$ (predicted value) and v (true value) is defined as

$$TI(\hat{v}, v, \alpha, \beta) = \frac{|\hat{v}v|}{|\hat{v}v| + \alpha\left|\hat{v}/v\right| + \beta\left|v/\hat{v}\right|} \tag{12}$$

where α and β control the magnitude of the penalties for false-positive and false-negative pixels, respectively.

H. Accuracy Assessment

This study assessed the result of the WFBM using numerical and visual analyses with a reference dataset. Due to the role of the reference map in assessing the result of WFBM, this study was designed to generate the reference map with high reliability. The reference data was generated by a native expert based on visual interpretation of the very high-resolution data and WFBM reports presented on some websites. Standard accuracy assessment indices were used for numerical accuracy assessment, which include overall accuracy, kappa coefficient, F1-score, recall, Jaccard index, precision, and balanced accuracy.

To evaluate the performance of QMDNN-Net, a novel state-of-the-art deep-learning-based method was also implemented. This is a CNN-based method that was proposed by Belenguer-Plomer *et al.* [47] for WFBM and that provided high efficiency

TABLE II
NUMBER OF SAMPLES USED FOR THE BURNED-AREA MAPPING FOR THE TWO STUDY AREAS

Study area	N° all samples	Class	N° samples	Data		
				Training	Validation	Testing
First	8,980,873	Unburned	6185	4,020	928	1,237
		Burned	13827	8,987	2,075	2,765
Second	47,000,184	Unburned	4970	3,230	745	995
		Burned	5308	3,450	797	1,061

in the different areas. More details of this CNN-based method can be found in [47].

IV. EXPERIMENTS AND RESULTS

The QMDNN-Net method is applied in the supervised learning framework that is required to sample data. We collected the sample dataset as randomized and systematic. In addition, Table II shows the details of the incorporated sample data for the two study areas. It can be noted that the collected sample data are $<1\%$ of the whole dataset. The sample data is divided into three parts: the training, validation, and testing data, as 65%, 15%, and 20%, respectively, of the whole sample dataset.

A. Parameter Settings

The parameter τ is defined by trial-and-error, which is here set to 4.0. The QMDNN-Net method has hyperparameters that it needs to set, which are set manually based on trial and error. The optimum values of these parameters are set as follows: input patch-size for Sentinel-2 and Sentinel-1 multitemporal coherence datasets, $13\times13\times10$ and $13\times13\times8$, respectively; initial learning rate 10^{-4}; number of neurons at the fully-connected layer, 1500; mini-batch size, 900; and number of iterations, 1500 (epochs). It is worth noting that the effects of these parameters on the performance of the network are low; e.g., the change in patch size from 11×11 to 13×13 only increases the accuracy of the network by 0.5%.

B. Results

This section investigates the result of WFBM using the QMDNN-Net method for two study areas. The two scenarios were designed to evaluate the efficiency of the QMDNN-Net method, using only the Sentinel-2 dataset and using the Sentinel-1 and Sentinel-2 fusion datasets.

1) First Study Area: The results of the WFBM for the first study area are shown in Fig. 10. As can be seen, the QMDNN-Net method showed good detection Fig. 10(b) and (c), and it is clear that other CNN-based method has high false pixels [see Fig. 10(a)]. While this issue can also be seen in the results of the QMDNN-Net method, this effect is lower than for the other methods [see Fig. 10(c)]. The QMDNN-Net method also provides considerable improvement in the WFBM by fusion of the multitemporal Sentinel-1 coherence map and the Sentinel-2 optical imagery, which relates mainly to around the burned areas. This improved efficiency is more evident in the detection of the *Unburned* pixels that can be seen for the whole study area.

Fig. 11 illustrates the confusion matrices of the WFBM for the first study area. The results were obtained by visual analysis of the data in Fig. 10. Among the 3555268 total ground truth *Unburned* pixels, the QMDNN-Net method detected 3193267 and 3427761 *Unburned* pixels for only the Sentinel-2 dataset and for the Sentinel-1 and Sentinel-2 fusion dataset, respectively, while the CNN-based method detected 3170464 *Unburned* pixels. Thus, in the fusion scenario, the QMDNN-Net method has the lowest *Unburned* error pixels, at 127507, compared to the CNN-based method with 384804 error pixels. It is also worth noting that for the 5425604 total ground truth *Burned* pixels, the CNN-based method shows 5160187 *Burned* pixels, while for the fusion scenario, the QMDNN-Net method provides fewer, at 5088568. Thus the CNN-based method provides better performance compared to the QMDNN-Net for the detection of *Burned* pixels, while it significantly misses its performance in the mapping of the *Unburned* pixels.

The numerical results of the mapping of the burned areas in terms of the quality measurement indices for the first study area are presented in Table III. These show that all of the methods provide an overall accuracy $>92\%$. The QMDNN-Net method outperformed the CNN-based method according to most of the indices, using either only the Sentinel-2 dataset or the Sentinel-1 and Sentinel-2 fusion dataset. The QMDNN-Net method improves the performance of the burned-area mapping by $>2\%$ according to the overall accuracy index. Furthermore, there is an improvement in most of the other indices, such as the Recall index, kappa coefficient, and Jaccard index. However, the CNN-based method provides greater precision compared to the QMDNN-Net method, although it does missed its performance for other indices. Additionally, the QMDNN-Net method generally provides improved performance with the fusion of the multitemporal coherence images and the optical Sentinel-2 datasets.

2) Second Study Area: The results of the WFBM for the second study area are shown in Fig. 12, where it can be seen that all of the methods provide good results for the detection of the burned areas. The main challenge among the methods is the correct mapping of the unburned pixels. There are many pixels that are classified as *Burned* pixels when they should be *Unburned* pixels. The CNN-based method shows many false pixels around the burned region. However, the QMDNN-Net method shows good detection compared to the other methods for both of its scenarios. The QMDNN-Net provides good performance in the second scenario [see Fig. 12(c)], while some noisy labeled pixels can be seen in the first scenario [see Fig. 12(b)].

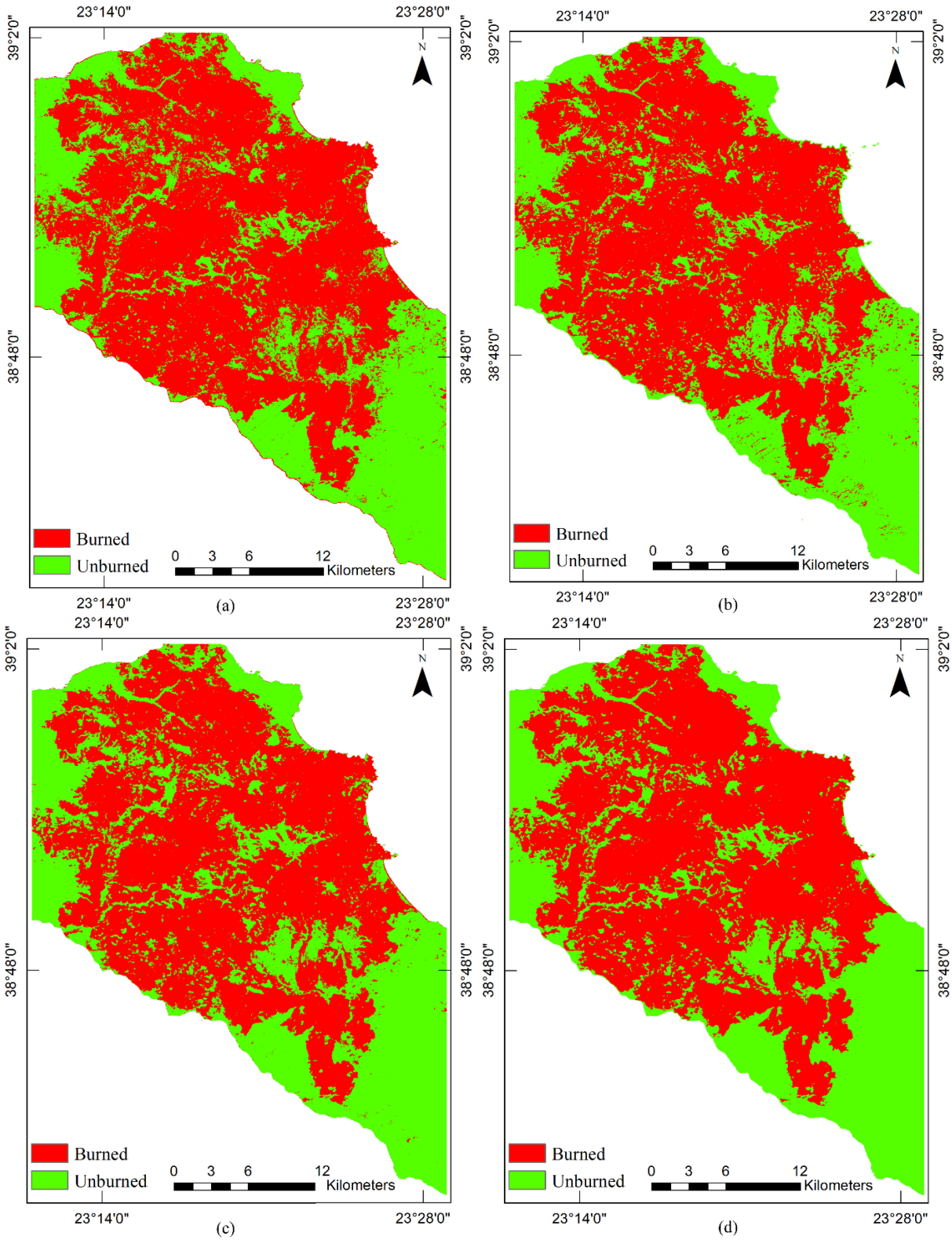

Fig. 10. Maps for visual comparisons of the results of WFBM based on the post/pre-event Sentinel-2 imagery for the first study area. (a) CNN-based method of [47]. (b) Proposed QMDNN-Net method using just the Sentinel-2 dataset. (c) Proposed QMDNN-Net method using the Sentinel-2 and SAR dataset. (d) Ground truth map.

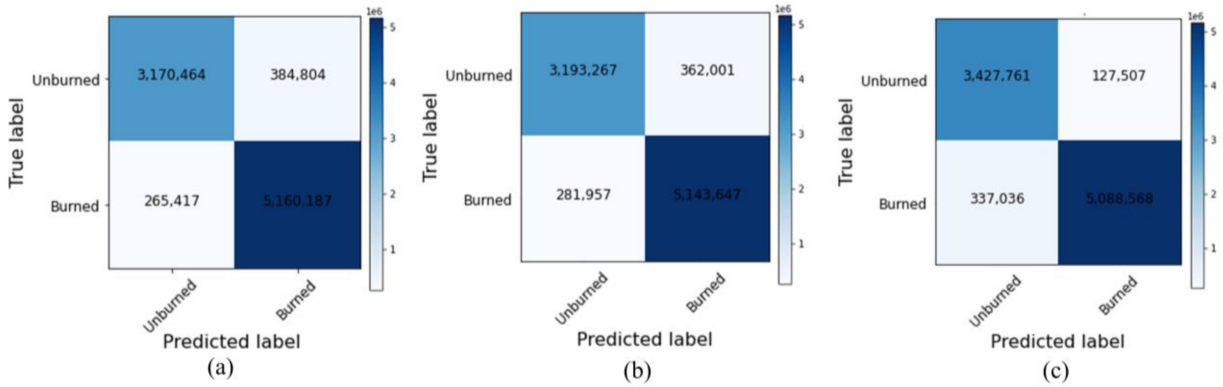

Fig. 11. (a) Comparison of the confusion matrices for the CNN-based method of [47], (b) the proposed QMDNN-Net method using just the Sentinel-2 dataset, and (c) using the Sentinel-1 and Sentinel-2 fusion dataset.

TABLE III
ACCURACY ASSESSMENT OF THE WFBM FOR THE FIRST STUDY AREA

Quality index	CNN-based method [47]	QMDNN-Net datasets	
		Sentinel-2 only	Sentinel-1/2 fusion
Overall accuracy (%)	92.75	92.83	94.82
Precision	92.27	91.88	91.05
Recall	89.17	89.81	96.41
F1-score (%)	90.69	90.84	93.65
Balanced accuracy	92.14	92.31	95.10
Jaccard index	0.829	0.831	0.881
Kappa coefficient	0.847	0.849	0.892

TABLE IV
ACCURACY ASSESSMENT OF THE WFBM FOR THE SECOND STUDY AREAS

Quality index	CNN-based method [47]	QMDNN-Net datasets	
		Sentinel-2 only	Sentinel-1/2 fusion
Overall accuracy (%)	93.58	97.13	**97.39**
Precision	99.26	98.67	98.96
Recall	93.18	97.96	**97.98**
F1-score (%)	96.12	98.32	**98.46**
Balanced accuracy	94.54	95.11	**95.96**
Jaccard index	0.925	0.967	**0.970**
Kappa coefficient	0.774	0.886	**0.897**

The confusion matrix of the results for the second study area is shown in Fig. 13. Here, the QMDNN-Net method shows better efficiency for the classification of the *Unburned* pixels, where it correctly defines more than 39369089 pixels from 40186532 total ground truth pixels using only the Sentinel-2 dataset. Furthermore, the QMDNN-Net method improved upon this performance of detection of the *Unburned* pixels in the fusion dataset (i.e., 39374292 *Unburned* pixels correctly identified). However, the CNN-based method provides some improvement in the detection of the *Burned* pixels, although this benefit is small in comparison with the error pixels in the *Unburned* class.

The quality indices for these numerical results for the WFBM methods for the second study area are presented in Table IV. Here, the two methods provide overall accuracies of >93%, although the QMDNN-Net method provides greater accuracy than the CNN-based method for most of these indices. Indeed, the QMDNN-Net method improves the accuracy mapping by >4% in terms of overall accuracy and the Recall index. Furthermore, there is a significant improvement for the WFBM using the QMDNN-Net method according to the kappa coefficient. Finally, while the CNN-based method provides slightly better performance according to the precision index, this benefit is lost for the other indices.

3) Comparison With the Landsat-8 Burned-Area Product: The Landsat-8 burned-area product is generated based on the normalized burned ratio thermal index with a temporal resolution of eight-days for the whole world. This index is defined by the near-infrared, the short-wave infrared, and the thermal band, and it requires thresholding, which is set here to 0.92 for discrimination between the burned areas (<0.92) and the

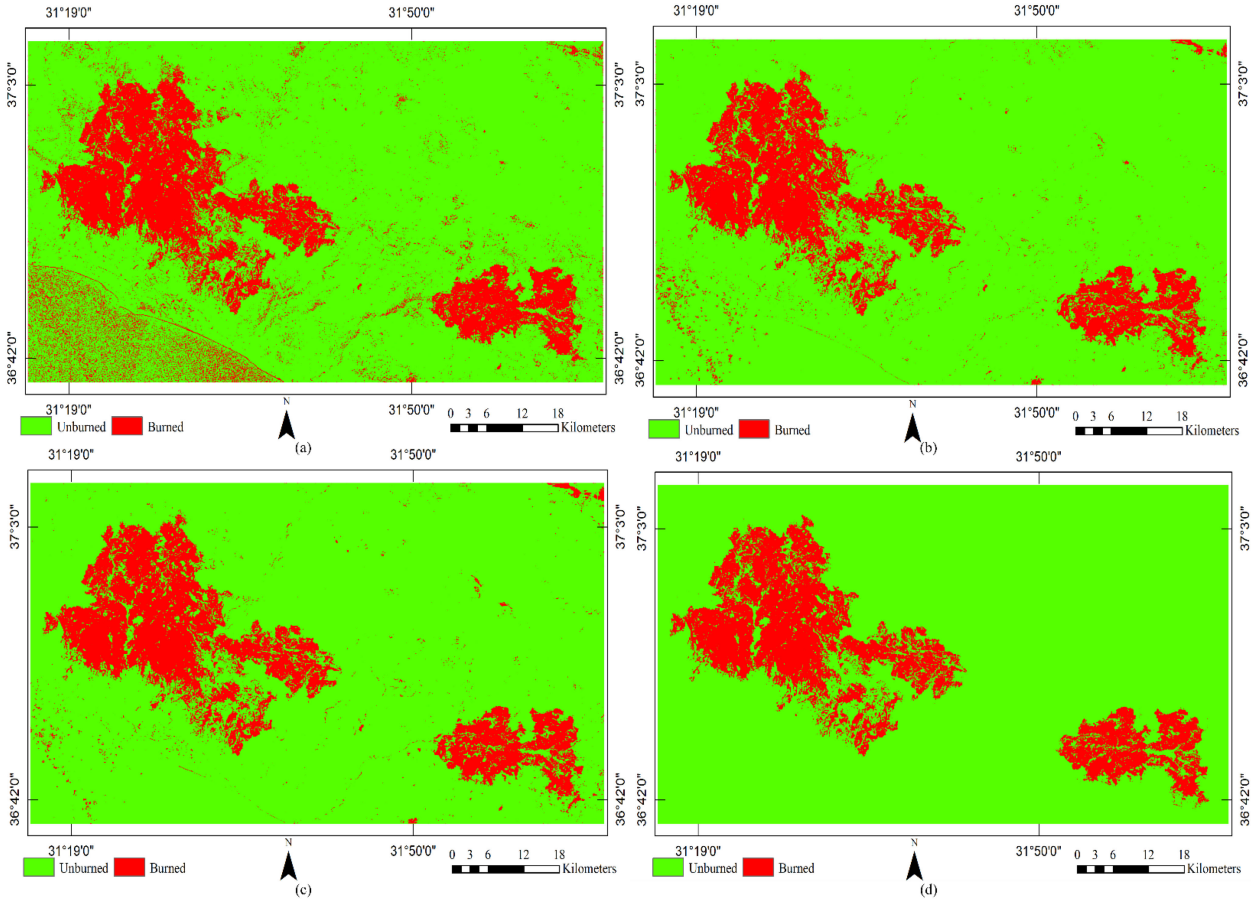

Fig. 12. Maps for visual comparison of the results of WFBM based on the post/pre-event Sentinel-2 imagery for the second study area. (a) CNN-based method of [47]. (b) Proposed QMDNN-Net method using just the Sentinel-2 dataset. (c) Proposed QMDNN-Net method using the Sentinel-2 and SAR dataset. (d) Ground truth map.

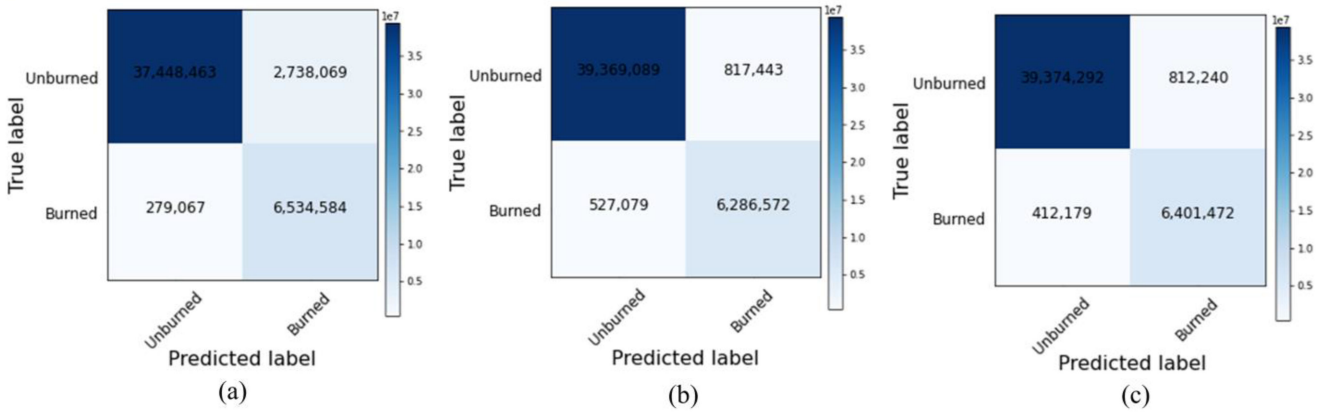

Fig. 13. (a) Comparison of the confusion matrices for the CNN-based method of [47], (b) proposed QMDNN-Net method using just the Sentinel-2 dataset, and (c) using the Sentinel-1 and Sentinel-2 fusion dataset.

unburned areas (>0.92). Fig. 14 shows the result of the WFBM using the QMDNN-Net method and the Landsat-8 burned-area product for the first study area. Fig. 14(b) shows the burned-area map generated by the Landsat-8 burned-area product, which shows that there are many missed pixels.

Here, the result of the WFBM using the QMDNN-Net method and the Landsat-8 burned-area product for the second study area are shown in Fig. 15. Similar to the QMDNN-Net method [see Fig. 15(b)], the Landsat-8 burned-area products have high efficiency in the mapping of the unburned areas; however, again, many of the burned pixels are missed. Thus, there are many burned pixels that are detected by the QMDNN-Net method that are not detected using the Landsat-8 burned-area product.

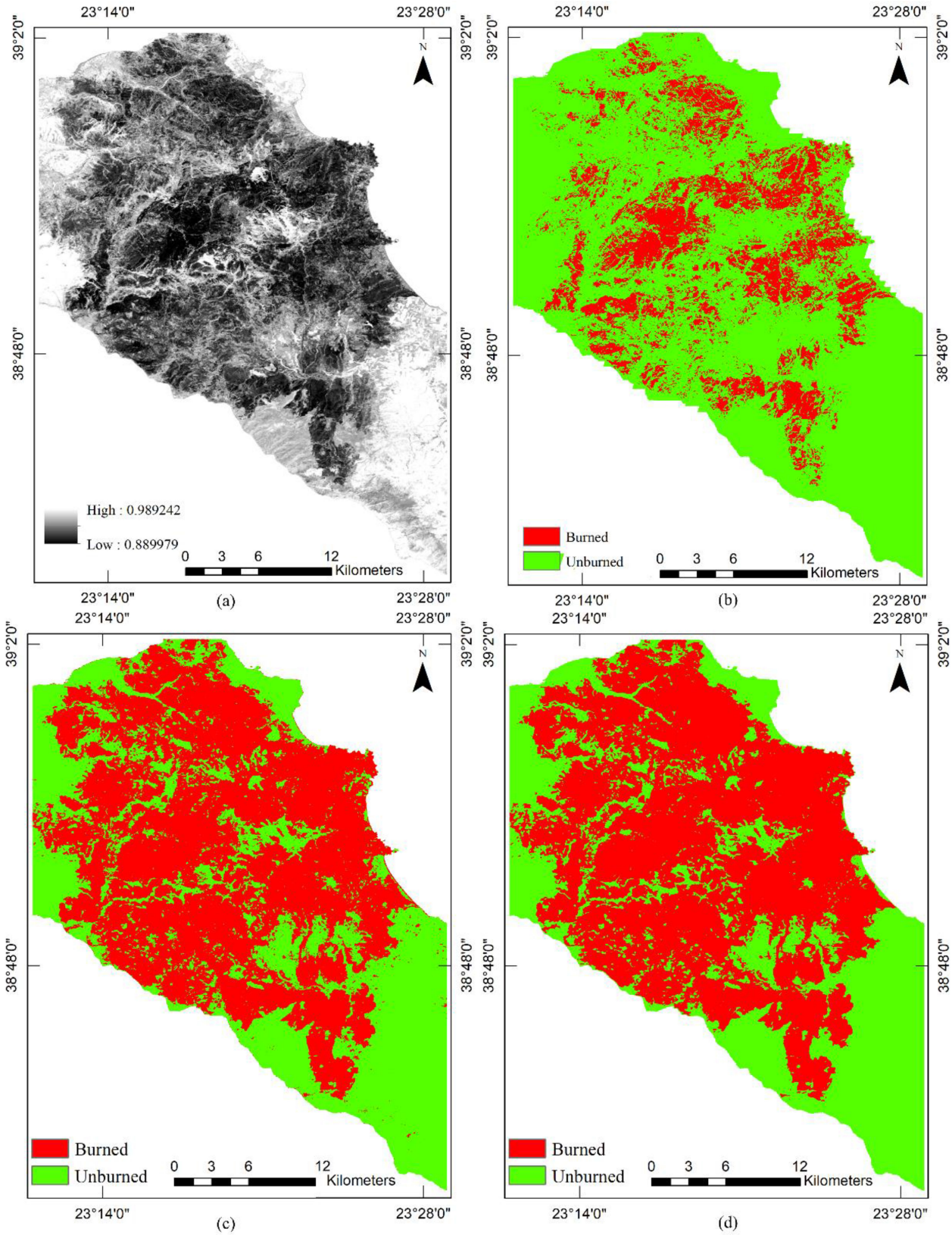

Fig. 14. Maps for visual comparison of the results of WFBM based on the Landsat-8 product for the first study area. (a) Derived Landsat-8 burned area product. (b) Landsat-8 burned-area product after thresholding. (c) QMDNN-Net method. (d) Ground truth map.

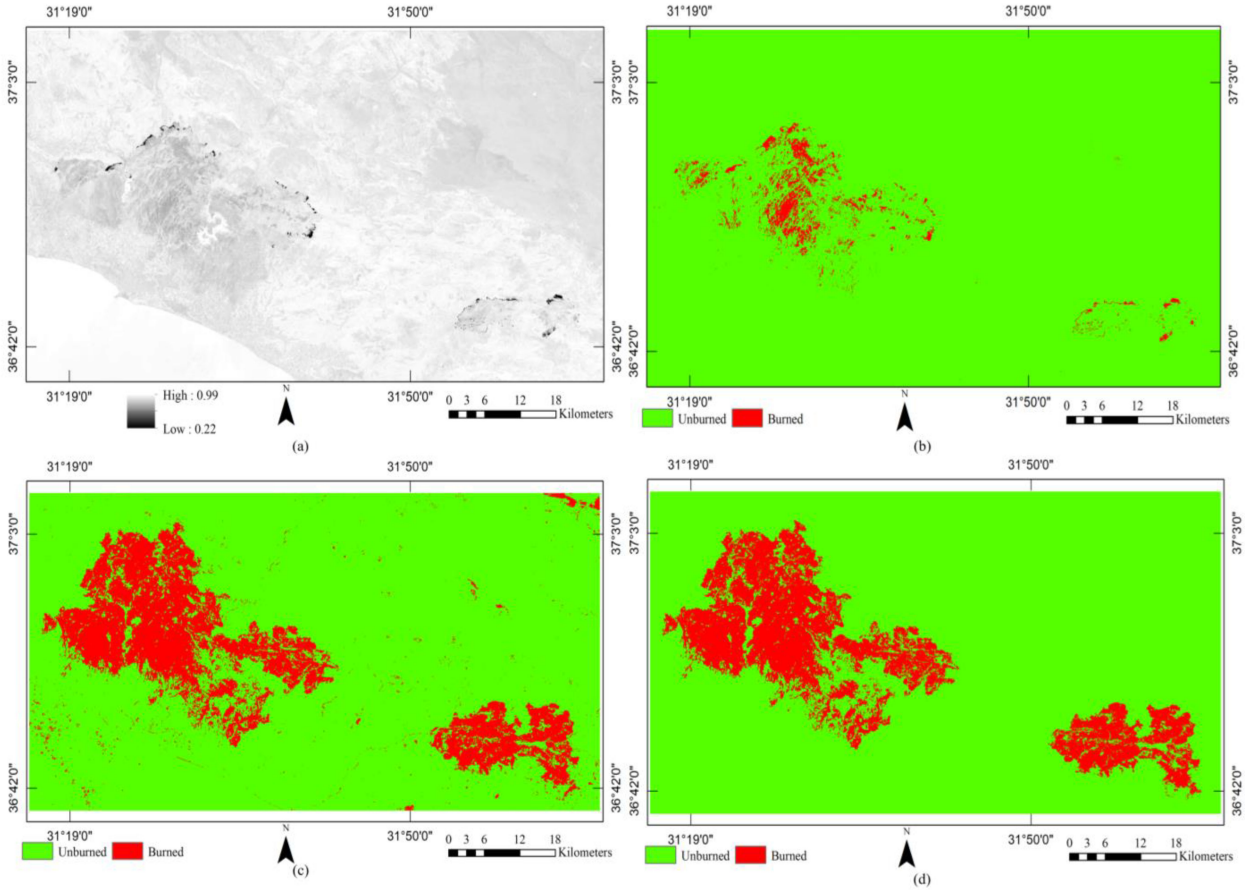

Fig. 15. Maps for visual comparison of the results of WFBM based on the Landsat-8 product for the second study area. (a) Derived Landsat-8 burned area product. (b) Thresholding the Landsat-8 burned-area product. (**c**) QMDNN-Net method. (d) Ground truth map.

TABLE V
ACCURACY ASSESSMENT OF THE WFBM FOR THE TWO STUDY AREAS

Quality index	First study area		Second study area	
	Landsat-8 product	QMDNN-Net fusion	Landsat-8 product	QMDNN-Net fusion
Overall accuracy (%)	60.87	**94.82**	86.36	**97.39**
Precision	50.29	**91.05**	86.69	**98.96**
Recall	**99.97**	96.41	**99.29**	97.98
F1-score (%)	66.92	**93.65**	92.56	**98.46**
Balanced accuracy	67.61	**95.10**	54.70	**95.96**
Jaccard index	0.502	**0.881**	0.861	**0.970**
Kappa coefficient	0.301	**0.892**	0.145	**0.897**

The confusion matrices for the WFBM are presented in Fig. 16, for both of the study areas. Here, it can be seen that the QMDNN-Net method shows significant improvement in the detection of the burned pixels, while the Landsat-8 burned-area product shows high levels of missed detection. Indeed, there are more than 20 00 000 missed burned detection pixels using the Landsat-8 burned-area product.

Table V presents the comparisons of the numerical results of the WFBM for both of the study areas. As can be seen, using the Sentinel-1 and Sentinel-2 fusion dataset, the QMDNN-Net method has higher efficiency than the Landsat-8 burned-area product. Indeed, the Landsat-8 burned-area product shows an overall accuracy as low as 60% (first study area), while the QMDNN-Net method has a corresponding overall accuracy of >94%. Thus, while the Landsat-8 burned-area product shows higher efficiency for mapping the unburned areas than the QMDNN-Net method, its performance is greatly reduced by the lower efficiency for mapping the Burned areas. Considering the balanced accuracy and F1-score as particularly important factors to define the results here, it can be seen that the QMDNN-Net method is significantly higher for both of these scores, compared to the Landsat-8 burned-area product.

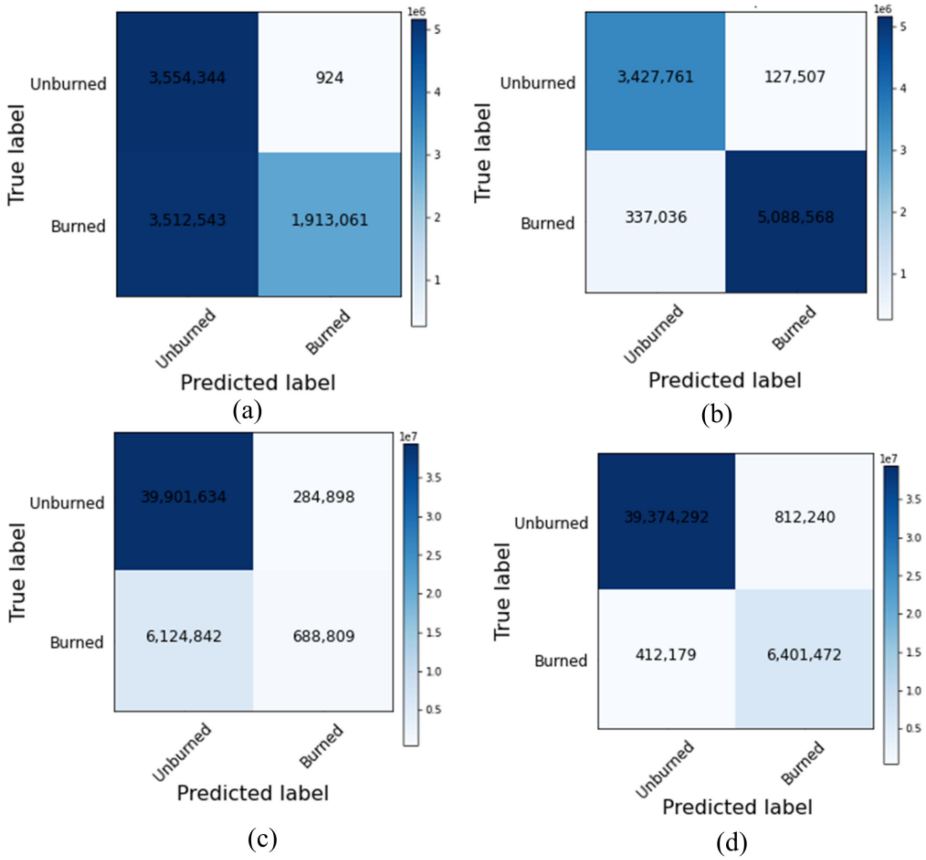

Fig. 16. Comparison of the confusion matrices for both of the study areas. (a, c) Landsat-8 burned-area product for the first (a) and second (c) study areas. (b, d) Proposed QMDNN-Net method using the Sentinel-1 and Sentinel-2 fusion dataset for the first (b) and second (d) study areas.

V. Discussion

Accurately and timely detection of burned areas are the most important factors in WFBM damage assessment. This study presents a novel framework for the mapping of burned areas based on Sentinel-2 and Sentinel-1 imagery. Analysis for WFBM has been conducted based on low-resolution imagery, such as Sentinel-3 and MODIS, due to the high temporal resolution, with many burned-area products now generated daily on a global scale. Fig. 17 illustrates the results of the MODIS burned-area products for the two study areas considered here. As can be seen here, although the MODIS burned-area products show lower noisy labeled pixels, they also show high missed detection and false pixels. For example, in Fig. 17(a), the MODIS burned-area product for the first study area shows many small unburned regions that have not been detected. Furthermore, Fig. 17(c) shows that the MODIS burned-area product for the second study area also shows many missed detection pixels. As a result, the MODIS burned-area product cannot detect burned areas well, due to some specific factors (i.e., coarse spatial resolution, weakness of the burned-area algorithm). Therefore, these products are suitable for global-scale analysis, but not for local and accurate WFBM.

The Landsat-8 burned-area product is another high-resolution product that covers the global scale with eight-day spatial resolution. Based on the numerical and visual analyses shown in Fig. 14 and 15 and in Table V, the Landsat-8 burned-area product shows many missed detection pixels. This depends on a number of factors, one of which is the complexity of the background, which means that a single global threshold cannot discriminate all of the burned areas. Thus, the detection of burned areas with only one burned ratio index is difficult. Furthermore, the selection of a suitable threshold for discriminating the burned areas is challenging.

Burned-area mapping by machine-learning methods has become more popular recently. The main advantages of machine-learning methods are the relatively low requirement for sample data and the ease of implementation. The strength of these methods depends on the quality of the input dataset and the features generated. Table VI gives an overview of WFBM using machine-learning methods. Most of these methods provide an overall accuracy of around 92% for small areas, while the QMDNN-Net method provides an overall accuracy of >94% for large-scale areas. Additionally, the generation of efficient spatial and spectral features is time-consuming, especially for large-scale areas. It is worth noting that Castillo *et al.* [70] provided an accuracy similar to the proposed method but this framework is based on manual feature extraction and thresholding. The finding of optimal threshold values for several features is time-consuming. Furthermore, due to the structure of forest areas and complexity of such areas, the threshold value is different from one case to other cases.

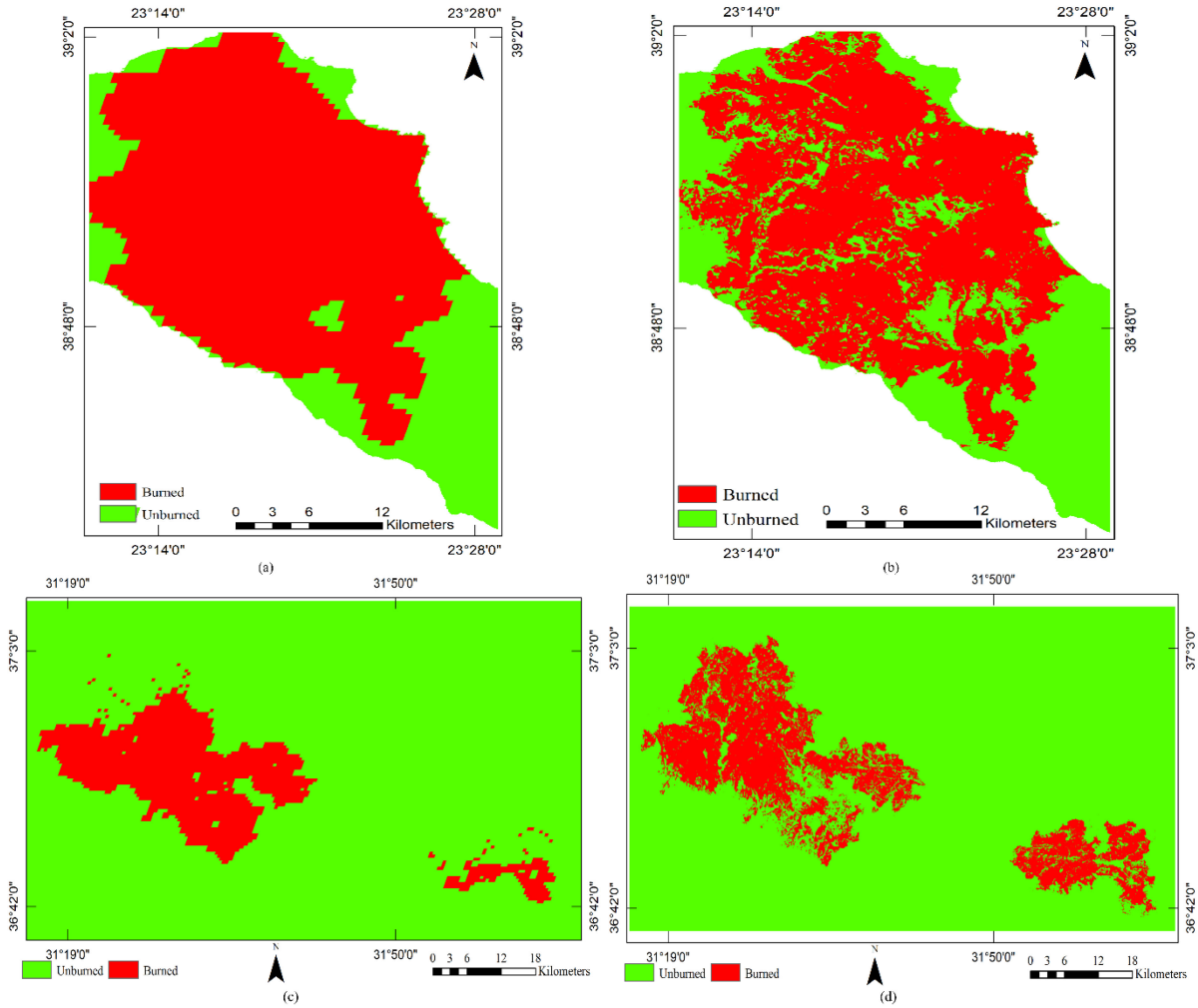

Fig. 17. Maps for visual comparison of the results of WFBM based on the MODIS burned-area product for the two study areas. (a, b) MODIS burned-area product for the first study area (a) and the corresponding ground truth map (b). (c, d) MODIS burned-area product for the second study area (c) and the corresponding ground truth map (d).

TABLE VI
COMPARISON OF THE PERFORMANCES OF QMDNN-NET COMPARED TO THE OTHER REPORTED BURNED-AREA MAPPING METHODS

Reference	Overall Accuracy(%)	Method	Dataset
[70]	94.5	Thresholding on spectral index	Sentinel-2
[20]	92	Support vector machine, imperialist competitive algorithm	Sentinel-2
[44]	92	Random forest change regression, in a region growing manner	Combined Landsat-8, Sentinel-2
[16]	91	Spectral and spatial features, random forest	Sentinel-2
QMDNN-Net	94.8	Deep-learning-based	Combined Sentinel-1, Sentinel-2

It is crucial for deep learning methods to perform an ablation analysis. Ablation analysis involves removing a section of the network to gain insight into how it affects the whole system. To this end, this research conducted the ablation analysis in three scenarios: (S#1) removing QM-block, (S#2) without GDC-block, and (S#3) QMDNN-Net with all functions. The result confusion matrices of ablation analysis of the proposed method are pretended in Fig. 18. As seen, the proposed method has provided better performance in the detection of the burned area by first and second scenarios compared with third scenario. The QMDNN-Net has high efficiency in the detection of unburned pixels by the first scenario (S#1). Furthermore, the QMDNN-Net method has provided considerable performance in the detection of burned pixels while missing the efficiency in the detection of

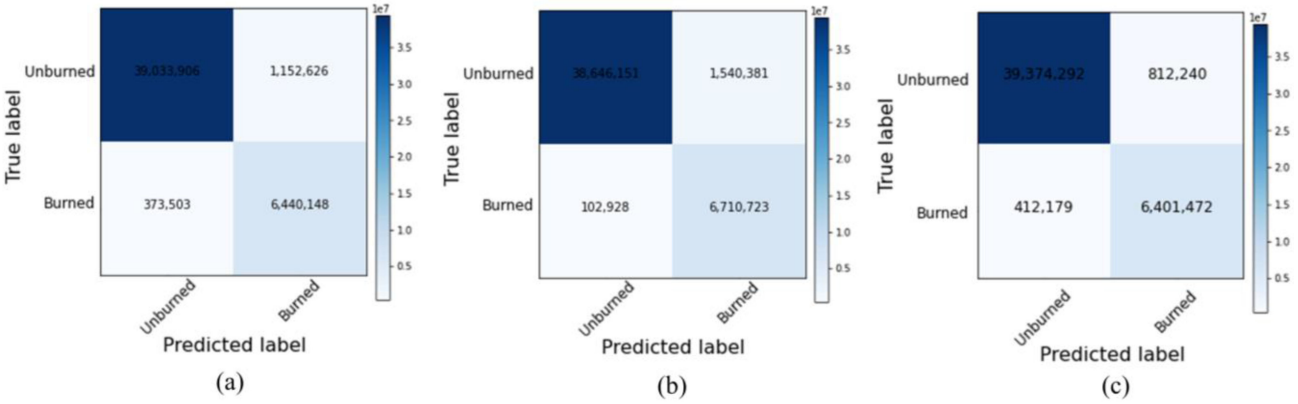

Fig. 18. Ablation analysis of the proposed method for the second study areas in the different scenarios. (a) Without QM-block (S#1), (b) without GDC-block (S#2), and (c) QMDNN-Net with all functions (S#3).

TABLE VII
ABLATION ANALYSIS OF THE PROPOSED NETWORK FOR THE SECOND DATASET

Quality index	Scenarios		
	Without QM-block (S#1)	Without GDC-block (S#2)	QMDNN-Net with all functions (S#3)
Overall accuracy (%)	96.75	96.50	**97.39**
Precision	99.05	**99.73**	98.96
Recall	97.13	96.16	**97.98**
F1-score (%)	98.05	97.91	**98.46**
Balanced accuracy	95.82	**97.32**	95.96
Jaccard index	0.962	0.959	**0.970**
Kappa coefficient	0.874	0.870	**0.897**

unburned pixels (false pixels are more than 15 40 000 pixels). Thus, the QMDNN-Net has improved the result by combining the QM-block and GDC-block as it reduces the miss detection and false pixels.

The results of the ablation analysis for the second dataset in three scenarios are shown in Table VII. As seen, the performance of QMDNN-Net is better than the other two scenarios by the most accurate assessment indices (i.e., overall accuracy, Recall, F1-score, Jaccard index, and Kappa coefficient). It is worth noting that the proposed method has provided the accuracy a bit better than both scenarios by Precision and Balanced accuracy but it considerably miss the performance by other accuracy assessment indices (i.e., Recall, Jaccard index, and Kappa coefficient). There is, however, a tradeoff between detecting burned and unburned samples that the ideal case is when a model can effectively classify both classes with minimum classification error.

This study proposes a novel framework based on hybrid QM layers and GDC blocks for mapping burned areas. Based on the results presented here for two large-scale areas, the proposed QMDNN-Net method outperforms the other state-of-the-art deep-learning-based WFBM methods. The strength of the QMDNN-Net method is its use of GDC-block and morphological layers that can detect burned areas with high complexity. This QMDNN-Net method is additive with high-resolution datasets that help the accurate mapping of burned area. The QMDNN-Net method combines the Sentinel-2 and multitemporal Sentinel-1 coherence dataset for the mapping of burned areas, which improves the efficiency of this WFBM by $>2\%$ according to the overall accuracy index.

One of the main advantages is that the QMDNN-Net method requires few sample data, as the sample data used represents $<1\%$ of the whole of the dataset. However, semantic segmentation-based methods (e.g., U-Net, DeeplabV3+) [13], [35] have provided promising results for many applications, although it is worth noting that these require large sample datasets. The collection of sample data is the most challenging aspect of supervised learning methods, especially for WFBM. Furthermore, these methods need more time for the tuning of their parameters, as this is time-consuming and challenging.

The fusion of remote sensing datasets by deep-learning methods can be applied at different levels, such as shallow feature levels and high feature levels. It has been shown that high feature level fusion can improve the efficiency of deep-learning-based methods. To this end, this study proposed a novel framework for fusion at a high deep-feature level based on a double stream deep-feature extractor. The Sentinel-2 and multitemporal coherence images are investigated using these channels, and then they are fused in the latest layers by concatenation. The double stream led to the extraction of a high-level feature map from the original dataset that uses the full potential of each of the datasets.

The generalisation capacity is the most important factor among the deep-learning-based methods. Unlike many

deep-learning-based methods, the QMDNN-Net method has a high generalisation capacity due to its structure. For example, there is a waterbody area and agricultural farms in the second dataset in the present study that are not included in the sample datasets. Thus, the proposed QMDNN-Net method provides good performance in such areas, while they are unseen in the sample data.

VI. Conclusion

Accurate and timely WFBM can help damage assessment and better management of such disasters. In this study, we propose a novel framework for WFBM that combines QM layers and convolution layers. Post-event Sentinel-2 and multitemporal coherence images are used for this burned-areas mapping for two large-scale regions. The performance of the QMDNN-Net method is compared here with other state-of-the-art methods and some burned-area products. The results of this WFBM show that the proposed QMDNN-Net algorithm has high efficiency in the mapping of burned areas. Furthermore, the fusion of post-event Sentinel-2 images with multitemporal Sentinel-1 coherence datasets can improve the results of this WFBM and reduce the false pixel levels.

The fusion of the Sentinel-1 and Sentinel-2 datasets also helps to map the burned areas in more detail and with more precision. Based on visual and numerical analyses, the burned-area products originated from MODIS and the Landsat-8 burned-area products show high missed detection of pixels and low accuracy in comparison with the Sentinel-based results. Furthermore, they have a low spatial resolution, while the QMDNN-Net method has a high spatial resolution.

The QMDNN-Net method has several particular benefits compared to other burned-area mapping methods

1) it provides high accuracy (>95%) in the mapping of burned areas;
2) the fusion of the Sentinel-2 and Sentinel-1 coherence datasets provides a high feature level based on double deep-feature extractor streams;
3) it requires relatively few sample data;
4) it combines the morphological and convolutional layers, which increases the efficacy of the network for WFBM in highly complex areas;
5) it has high generalization capabilities over various study areas.

In spite of the fact that it took longer to train QMEM-Net compared to other deep learning methods (i.e., one hour more), the proposed method was chosen due to its higher accuracy and more robust results.

References

[1] S. J. Prichard *et al.*, "Adapting western North American forests to climate change and wildfires: 10 common questions," *Ecol. Appl.*, vol. 31, 2021, Art. no. e02433.

[2] C. S. Stevens-Rumann *et al.*, "Evidence for declining forest resilience to wildfires under climate change," *Ecol. Lett.*, vol. 21, no. 2, pp. 243–252, 2018.

[3] R. Xu *et al.*, "Wildfires, global climate change, and human health," *New England J. Med.*, vol. 383, no. 22, pp. 2173–2181, 2020.

[4] A. K. Magnan *et al.*, "Estimating the global risk of anthropogenic climate change," *Nature Climate Change*, vol. 11, no. 10, pp. 879–885, 2021.

[5] W. Tang *et al.*, "Widespread phytoplankton blooms triggered by 2019–2020 Australian wildfires," *Nature*, vol. 597, no. 7876, pp. 370–375, 2021.

[6] S. T. Seydi, M. Hasanlou, M. Amani, and W. Huang, "Oil spill detection based on multiscale multidimensional residual CNN for optical remote sensing imagery," *IEEE J. Sel. Topics Appl. Earth Observ. Remote Sens.*, vol. 14, pp. 10941–10952, Oct. 2021.

[7] U. A. Bhatti *et al.*, "Local similarity-based spatial-spectral fusion hyperspectral image classification with deep CNN and Gabor filtering," *IEEE Trans. Geosci. Remote Sens.*, vol. 60, Sep. 2022, Art. no. 5514215.

[8] X. Wu, D. Hong, and J. Chanussot, "Convolutional neural networks for multimodal remote sensing data classification," *IEEE Trans. Geosci. Remote Sens.*, vol. 60, Nov. 2022, Art. no. 5517010.

[9] J. Xie, L. Fang, B. Zhang, J. Chanussot, and S. Li, "Super resolution guided deep network for land cover classification from remote sensing images," *IEEE Trans. Geosci. Remote Sens.*, vol. 60, Oct. 2022, Art. no. 5611812.

[10] J. G. Pausas and J. E. Keeley, "Wildfires and global change," *Front. Ecol. Environ.*, vol. 19, pp. 387–395, 2021.

[11] S. T. Seydi, R. Shah-Hosseini, and M. Hasanlou, "New framework for hyperspectral change detection based on multi-level spectral unmixing," *Appl. Geomatics*, vol. 13, pp. 763–780, 2021.

[12] P. Zhang, Y. Ban, and A. Nascetti, "SAR-Based wildfire progression mapping withTotal-Variation regularized transfer learning," *IEEE Trans. Geosci. Remote Sens.*, 2021.

[13] P. Zhang, Y. Ban, and A. Nascetti, "Learning U-Net without forgetting for near real-time wildfire monitoring by the fusion of SAR and optical time series," *Remote Sens. Environ.*, vol. 261, 2021, Art. no. 112467.

[14] Y. Xi, S. Peng, P. Ciais, and Y. Chen, "Future impacts of climate change on inland Ramsar wetlands," *Nature Climate Change*, vol. 11, no. 1, pp. 45–51, 2021.

[15] W. Taylor *et al.*, "High altitude hunting, climate change, and pastoral resilience in eastern Eurasia," *Sci. Rep.*, vol. 11, no. 1, pp. 1–13, 2021.

[16] S. T. Seydi, M. Akhoondzadeh, M. Amani, and S. Mahdavi, "Wildfire damage assessment over Australia using sentinel-2 imagery and MODIS land cover product within the Google Earth Engine cloud platform," *Remote Sens.*, vol. 13, no. 2, p. 220, 2021.

[17] E. Chuvieco *et al.*, "Historical background and current developments for mapping burned area from satellite earth observation," *Remote Sens. Environ.*, vol. 225, pp. 45–64, 2019.

[18] J. A. Rodrigues *et al.*, "How well do global burned area products represent fire patterns in the Brazilian Savannas biome? An accuracy assessment of the MCD64 collections," *Int. J. Appl. Earth Observ. Geoinf.*, vol. 78, pp. 318–331, 2019.

[19] D. Rashkovetsky, F. Mauracher, M. Langer, and M. Schmitt, "Wildfire detection from multisensor satellite imagery using deep semantic segmentation," *IEEE J. Sel. Topics Appl. Earth Observ. Remote Sens.*, vol. 14, pp. 7001–7016, Jun. 2021.

[20] M. Syifa, M. Panahi, and C.-W. Lee, "Mapping of post-wildfire burned area using a hybrid algorithm and satellite data: The case of the camp fire wildfire in california, USA," *Remote Sens.*, vol. 12, no. 4, p. 623, 2020.

[21] S. Liu, Y. Zheng, M. Dalponte, and X. Tong, "A novel fire index-based burned area change detection approach using Landsat-8 OLI data," *Eur. J. Remote Sens.*, vol. 53, no. 1, pp. 104–112, 2020.

[22] L. Boschetti, D. P. Roy, C. O. Justice, and M. L. Humber, "MODIS–Landsat fusion for large area 30 m burned area mapping," *Remote Sens. Environ.*, vol. 161, pp. 27–42, 2015.

[23] L. A. Hardtke, P. D. Blanco, H. F. del Valle, G. I. Metternicht, and W. F. Sione, "Semi-automated mapping of burned areas in semi-arid ecosystems using MODIS time-series imagery," *Int. J. Appl. Earth Observ. Geoinf.*, vol. 38, pp. 25–35, 2015.

[24] T. J. Hawbaker *et al.*, "Mapping burned areas using dense time-series of Landsat data," *Remote Sens. Environ.*, vol. 198, pp. 504–522, 2017.

[25] B. Jakimow, P. Griffiths, S. van der Linden, and P. Hostert, "Mapping pasture management in the Brazilian amazon from dense Landsat time series," *Remote Sens. Environ.*, vol. 205, pp. 453–468, 2018.

[26] L. Giglio, L. Boschetti, D. P. Roy, M. L. Humber, and C. O. Justice, "The collection 6 MODIS burned area mapping algorithm and product," *Remote Sens. Environ.*, vol. 217, pp. 72–85, 2018.

[27] E. Roteta, A. Bastarrika, M. Padilla, T. Storm, and E. Chuvieco, "Development of a Sentinel-2 burned area algorithm: Generation of a small fire database for sub-Saharan Africa," *Remote Sens. Environ.*, vol. 222, pp. 1–17, 2019.

[28] J. Lizundia-Loiola, G. Otón, R. Ramo, and E. Chuvieco, "A spatio-temporal active-fire clustering approach for global burned area mapping at 250 m from MODIS data," *Remote Sens. Environ.*, vol. 236, 2020, Art. no. 111493.

[29] M. M. Pinto, R. Libonati, R. M. Trigo, I. F. Trigo, and C. C. DaCamara, "A deep learning approach for mapping and dating burned areas using temporal sequences of satellite images," *ISPRS J. Photogram. Remote Sens.*, vol. 160, pp. 260–274, 2020.

[30] J. Liu, J. Heiskanen, E. E. Maeda, and P. K. Pellikka, "Burned area detection based on Landsat time series in savannas of southern Burkina Faso," *Int. J. Appl. Earth Observ. Geoinf.*, vol. 64, pp. 210–220, 2018.

[31] R. Llorens, J. A. Sobrino, C. Fernández, J. M. Fernández-Alonso, and J. A. Vega, "A methodology to estimate forest fires burned areas and burn severity degrees using Sentinel-2 data. Application to the October 2017 fires in the Iberian Peninsula," *Int. J. Appl. Earth Observ. Geoinf.*, vol. 95, 2021, Art. no. 102243.

[32] S. Urbanski *et al.*, "A VIIRS direct broadcast algorithm for rapid response mapping of wildfire burned area in the western United States," *Remote Sens. Environ.*, vol. 219, pp. 271–283, 2018.

[33] A. I. Cabral, S. Silva, P. C. Silva, L. Vanneschi, and M. J. Vasconcelos, "Burned area estimations derived from Landsat ETM+ and OLI data: Comparing genetic programming with maximum likelihood and classification and regression trees," *ISPRS J. Photogram. Remote Sens.*, vol. 142, pp. 94–105, 2018.

[34] R. Çömert, K. M. D., and U. Avdan, "Object based burned area mapping with random forest algorithm," *Int. J. Eng. Geosci.*, vol. 4, no. 2, pp. 78–87, 2019.

[35] A. Brand and A. Manandhar, "Semantic segmentation of burned areas in satellite images using a U-net-based convolutional neural network," *Int. Arch. Photogram. Remote Sens. Spatial Inf. Sci.*, vol. 43, pp. 47–53, 2021.

[36] E. Sertel and U. Alganci, "Comparison of pixel and object-based classification for burned area mapping using SPOT-6 images," *Geomatics, Natural Hazards Risk*, vol. 7, no. 4, pp. 1198–1206, 2016.

[37] F. Ngadze, K. S. Mpakairi, B. Kavhu, H. Ndaimani, and M. S. Maremba, "Exploring the utility of Sentinel-2 MSI and Landsat 8 OLI in burned area mapping for a heterogenous savannah landscape," *PLOS One*, vol. 15, no. 5, 2020, Art. no. e0232962.

[38] E. Dragozi, I. Z. Gitas, D. G. Stavrakoudis, and J. B. Theocharis, "Burned area mapping using support vector machines and the FuzCoC feature selection method on VHR IKONOS imagery," *Remote Sens.*, vol. 6, no. 12, pp. 12005–12036, 2014.

[39] R. Ba, W. Song, X. Li, Z. Xie, and S. Lo, "Integration of multiple spectral indices and a neural network for burned area mapping based on MODIS data," *Remote Sens.*, vol. 11, no. 3, p. 326, 2019.

[40] L. Knopp, M. Wieland, M. Rättich, and S. Martinis, "A deep learning approach for burned area segmentation with Sentinel-2 data," *Remote Sens.*, vol. 12, no. 15, 2020, Art. no. 2422.

[41] P. Wang, L. Zhang, G. Zhang, B. Jin, and H. Leung, "Multispectral image super-resolution burned-area mapping based on space-temperature information," *Remote Sens.*, vol. 11, no. 22, 2019, Art. no. 2695.

[42] Q. Zhang *et al.*, "Deep-learning-based burned area mapping using the synergy of Sentinel-1&2 data," *Remote Sens. Environ.*, vol. 264, 2021, Art. no. 112575.

[43] I. Alonso-Canas and E. Chuvieco, "Global burned area mapping from ENVISAT-MERIS and MODIS active fire data," *Remote Sens. Environ.*, vol. 163, pp. 140–152, 2015.

[44] D. P. Roy *et al.*, "Landsat-8 and Sentinel-2 burned area mapping-A combined sensor multi-temporal change detection approach," *Remote Sens. Environ.*, vol. 231, 2019, Art. no. 111254.

[45] M. A. Belenguer-Plomer, M. A. Tanase, A. Fernandez-Carrillo, and E. Chuvieco, "Burned area detection and mapping using Sentinel-1 backscatter coefficient and thermal anomalies," *Remote Sens. Environ.*, vol. 233, 2019, Art. no. 111345.

[46] M. A. Crowley, J. A. Cardille, J. C. White, and M. A. Wulder, "Multisensor, multi-scale, Bayesian data synthesis for mapping within-year wildfire progression," *Remote Sens. Lett.*, vol. 10, no. 3, pp. 302–311, 2019.

[47] M. A. Belenguer-Plomer, M. A. Tanase, E. Chuvieco, and F. Bovolo, "CNN-based burned area mapping using radar and optical data," *Remote Sens. Environ.*, vol. 260, 2021, Art. no. 112468.

[48] M. Main-Knorn, B. Pflug, J. Louis, V. Debaecker, U. Müller-Wilm, and F. Gascon, "Sen2Cor for sentinel-2," *Proc. SPI*, vol. 10427, 2017, Art. no. 1042704.

[49] J. Louis *et al.*, "Sentinel-2 Sen2Cor: L2A processor for users," in *Proc. Proc. Living Planet Symp.*, 2016, pp. 1–8.

[50] A. Pulella, F. Sica, and P. Rizzoli, "Monthly deforestation monitoring with sentinel-1 multi-temporal signatures and InSAR coherences," *Revista de Teledetección*, vol. 56, pp. 1–22, 2020.

[51] D. Mandal *et al.*, "Sentinel-1 SLC preprocessing workflow for polarimetric applications: A generic practice for generating dual-pol covariance matrix elements in SNAP S-1 toolbox," *Preprints*, Nov. 2019, doi: 10.20944/preprints201911.0393.v1.

[52] M. Hasanlou, R. Shah-Hosseini, S. T. Seydi, S. Karimzadeh, and M. Matsuoka, "Earthquake damage region detection by multitemporal coherence map analysis of radar and multispectral imagery," *Remote Sens.*, vol. 13, no. 6, 2021, Art. no. 1195.

[53] T. ElGharbawi and F. Zarzoura, "Damage detection using SAR coherence statistical analysis, application to Beirut, Lebanon," *ISPRS J. Photogram. Remote Sens.*, vol. 173, pp. 1–9, 2021.

[54] N. E. Huang *et al.*, "The empirical mode decomposition and the Hilbert spectrum for nonlinear and non-stationary time series analysis," *Proc. Roy. Soc. London. Ser. A, Math., Phys. Eng. Sci.*, vol. 454, no. 1971, pp. 903–995, 1998.

[55] S. Velasco-Forero, R. Pagès, and J. Angulo, "Learnable empirical mode decomposition based on mathematical morphology," vol. 19, pp. 387–395, 2021.

[56] S. T. Seydi, M. Hasanlou, and J. Chanussot, "DSMNN-Net: A deep siamese morphological neural network model for burned area mapping using multispectral sentinel-2 and hyperspectral PRISMA images," *Remote Sens.*, vol. 13, no. 24, 2021, Art. no. 5138.

[57] C. Yu, R. Han, M. Song, C. Liu, and C.-I. Chang, "A simplified 2D-3D CNN architecture for hyperspectral image classification based on spatial–spectral fusion," *IEEE J. Sel. Topics Appl. Earth Observ. Remote Sens.*, vol. 13, pp. 2485–2501, Apr. 2020.

[58] R. Mondal, "Morphological Network: Network with Morphological Neurons," Indian Statistical Institute-Kolkata, Kolkata, India, 2021.

[59] A. Kirszenberg, G. Tochon, É. Puybareau, and J. Angulo, "Going beyond p-convolutions to learn grayscale morphological operators," in *Proc. Int. Conf. Discrete Geometry Math. Morphol.*, 2021, pp. 470–482.

[60] M. Klemen, L. Krsnik, and M. Robnik-Šikonja, "Enhancing deep neural networks with morphological information," *Natural Lang. Eng.*, pp. 1–26, Feb. 2022.

[61] G. X. Ritter and P. Sussner, "An introduction to morphological neural networks," in *Proc. Int. Conf. Pattern Recognit.*, 1996, vol. 4, pp. 709–717.

[62] Y. Shen, X. Zhong, and F. Y. Shih, "Deep morphological neural networks," Sep. 2019, *arXiv:1909.01532*.

[63] S. K. Roy, R. Mondal, M. E. Paoletti, J. M. Haut, and A. Plaza, "Morphological convolutional neural networks for hyperspectral image classification," *IEEE J. Sel. Topics Appl. Earth Observ. Remote Sens.*, vol. 14, pp. 8689–8702, 2021.

[64] R. Duits, T. D. Haije, E. Creusen, and A. Ghosh, "Morphological and linear scale spaces for fiber enhancement in DW-MRI," *J. Math. Imag. Vis.*, vol. 46, no. 3, pp. 326–368, 2013.

[65] A. C. Jalba, M. H. Wilkinson, and J. B. Roerdink, "Shape representation and recognition through morphological curvature scale spaces," *IEEE Trans. Image Process.*, vol. 15, no. 2, pp. 331–341, Feb. 2006.

[66] B. Raducanu, M. Graña, and F. X. Albizuri, "Morphological scale spaces and associative morphological memories: Results on robustness and practical applications," *J. Math. Imag. Vis.*, vol. 19, no. 2, pp. 113–131, 2003.

[67] M. Welk, "Families of generalised morphological scale spaces," in *Proc. Int. Conf. Scale-Space Theories Comput. Vis.*, 2003, pp. 770–784.

[68] D. P. Kingma and J. Ba, "Adam: A method for stochastic optimization," Dec. 2014, *arXiv:1412.6980*.

[69] S. S. M. Salehi, D. Erdogmus, and A. Gholipour, "Tversky loss function for image segmentation using 3D fully convolutional deep networks," in *Proc. Int. Workshop Mach. Learn. Med. Imag.*, 2017, pp. 379–387.

[70] E. B. Castillo *et al.*, "Monitoring wildfires in the northeastern peruvian amazon using landsat-8 and sentinel-2 imagery in the GEE platform," *ISPRS Int. J. Geo-Inf.*, vol. 9, no. 10, p. 564, 2020.

Seyd Teymoor Seydi (Member, IEEE) received the B.Eng. degree in surveying and geomatics engineering from the University of Shahid Rajaei, Iran, in 2015, and the M.Eng. degree in remote sensing from the University of Tehran, Tehran, Iran, in 2018.

He serves as a regular reviewer in about five international remote sensing journals. A list of his research works, including over 35 peer-reviewed journal and conference papers. His research interests include multitemporal multispectral/hyperspectral and SAR remote sensing processing and classification, and advance deep learning algorithms.

Mahdi Hasanlou (Member, IEEE) received the B.Sc. degree in surveying and geomatics engineering from the University of Tehran, Tehran, Iran, in 2003, the M.Sc. degree in remote sensing from University of Tehran, Tehran, Iran, in 2006, and the Ph.D. degree in remote sensing from University of Tehran, Tehran, Iran, in 2013.

Since 2013, he has been an Assistant Professor with the School of Surveying and Geospatial Engineering, College of Engineering, University of Tehran, Iran, where he is the Head of the remote sensing laboratory, where he is currently the Head of the remote sensing and photogrammetry group at this school. His research interest includr hyperspectral, thermal, optical, and SAR remote sensing for urban and agro-environmental applications.

Jocelyn Chanussot (Fellow, IEEE) received the M.Sc. degree in electrical engineering from the Grenoble Institute of Technology (Grenoble INP), Grenoble, France, in 1995, and the Ph.D. degree in electrical engineering from the Universit de Savoie, Annecy, France, in 1998.

Since 1999, he has been with Grenoble INP, Grenoble, France, where he is currently a Professor of signal and image processing. He was a Visiting Scholar with Stanford University, Stanford, CA, USA, KTH, Stockholm, Sweden, and NUS, Singapore. Since 2013, he has been an Adjunct Professor with the University of Iceland, Reykjavik, Iceland, and the Chinese Academy of Sciences, Aerospace Information research Institute, Beijing, China. In 2015–2017, he was a Visiting Professor with the University of California, Los Angeles, Los Angeles, CA, USA. His research interests include image analysis, hyperspectral remote sensing, data fusion, machine learning, and artificial intelligence.

Prof. Chanussot holds the AXA Chair in remote sensing with the Chinese Academy of Sciences, Aerospace Information research Institute. He is the founding President of IEEE Geoscience and Remote Sensing French Chapter (2007–2010), which received the 2010 IEEE GRS-S Chapter Excellence Award. He was the recipient of multiple outstanding paper awards. He was the Vice-President of the IEEE Geoscience and Remote Sensing Society, in charge of meetings and symposia (2017–2019). He was the General Chair of the first IEEE GRSS Workshop on Hyperspectral Image and Signal Processing, Evolution in Remote Sensing. He was the Chair (2009–2011) and Co-Chair of the GRS Data Fusion Technical Committee (2005–2008). He was a member of the Machine Learning for Signal Processing Technical Committee of the IEEE Signal Processing Society (2006–2008) and the Program Chair of the IEEE International Workshop on Machine Learning for Signal Processing (2009). He is an Associate Editor for IEEE TRANSACTIONS ON GEOSCIENCE AND REMOTE SENSING, IEEE TRANSACTIONS ON IMAGE PROCESSING, and PROCEEDINGS OF THE IEEE. He was the Editor-In-Chief of IEEE JOURNAL OF SELECTED TOPICS IN APPLIED EARTH OBSERVATIONS AND REMOTE SENSING (2011–2015). In 2014, he was a Guest Editor for the IEEE Signal Processing Magazine. He is a Member of the Institut Universitaire de France (2012–2017) and a Highly Cited Researcher (Clarivate Analytics/Thomson Reuters).